Scope#10: Methodology for developing high-resolution stream and waterbody datasets for the Chesapeake Bay watershed

Report to Chesapeake Bay Trust

October 2018

Matthew Baker, mbaker@umbc.edu

David Saavedra, dsaavedra@chesapeakeconservancy.org

Michael Norton, mnorton@chesapeakeconservancy.org

Table of Contents

Introduction

Stream channel mapping, particularly in headwaters, is critical for a suite of environmental applications including hydrologic and hydraulic modeling, soil conservation, wetland conservation, water quality analysis, and regulatory policy (Montgomery and Dietrich 1988; Hancock and Evans 2006; Baker et al. 2007; Julian et al. 2012). However, accurate mapping of channel heads is a long-standing challenge in geomorphology, largely due to the fact that channels form as a result of several different processes and because human activity can drastically alter both key processes as well as the geomorphic evidence used as criteria for delineation (Rodriguez-Iturbe and Rinaldo 2001). The complexity and variety of channel features often defies easy categorization, even by skilled interpreters, and thus complicates attempts at automated channel delineation.

Improved automated tools are a practical necessity for accurate stream channel identification over broad landscapes, and the development of those tools has been an active subject of research for several decades. Although existing methods have achieved a great level of sophistication, they may also be prone to errors of both omission and commission. These errors occur in part because many existing methods try to detect idealized features derived from theory or empirical observations of natural landscapes that are ill-suited for landscapes altered by humans. The challenge lies in developing objective detection and mapping processes that extend across broad areas and adapt to different terrain or land use contexts. The current state-of-the-art in stream mapping techniques thus typically rely on direct-detection of channel-like features using terrain curvature (Wilson and Gallant 2000; Lashermes et al. 2007), or topographic openness (Yokoyama et al. 2002).

In this report, we present an approach for mapping stream headwaters utilizing *geomorphons*, a method that builds on concepts from computer vision to accurately classify terrain into discrete landform elements (Jasiewicz and Stepinski 2013). The geomorphon algorithm classifies each pixel in an elevation raster by assessing surrounding elevation along a line of sight in eight compass directions. Based on the arrangement of higher, lower, or equal elevations surrounding the focal cell, each pixel is classified into one of ten common landform elements, each referred to as a geomorphon. The ten landform elements include: flat, peak, ridge, shoulder, spur, slope, hollow, footslope, valley, and pit.

Geomorphons seamlessly incorporate geomorphic concepts like positive and negative openness. Further, stream channel delineation with geomorphons has many theoretical and practical advantages over other methods. In short, like many methods that directly interpret terrain features, geomorphons outperform other methods because they map “what is” rather than “what should be.” A key advantage of the geomorphon approach is its ability to identify features at multiple length-scales. The algorithm can be used to identify broad stream valleys and it can be constrained to identify stream channels within those valleys. In addition, the application of geomorphons for mapping stream channels is straightforward and computationally efficient.

To provide verification for the approach developed in this work, the project team visited 14 different field sites around the Chesapeake Bay watershed located in five different physiographic provinces: Appalachian Plateau, Valley and Ridge, Blue Ridge, Piedmont, and Coastal Plain. The data collected on these field visits provided on-the-ground context for the manner in which channels form and behave in different geographies and an evaluation of the applicability of various mapping methods. We use field data to compare the relative performance of geomorphons with other direct-detection techniques for accurately identifying the locations of channel heads.

This report is structured as follows: First, we present a literature review that links both mechanisms by which channels form and existing methods by which they are detected. Second, a methods section reviews the technical steps that we used to build stream maps at the 14 field sites, including comparing different approaches for detecting stream heads, as well as cartographic and geomorphic approaches for removing spurious detections and constructing a channel network. Third, a results section describes characteristics of the various outputs and details their relative performance for identifying and linking stream heads at the 14 field sites. Lastly, we conclude with recommendations including potential for improvement and next steps forward.

Literature Review

Channel formation

There are several distinct natural mechanisms by which stream channels form. Channel heads result from hydraulic erosion from overland flow (saturation or Hortonian), seepage erosion where subsurface water intersects the land surface, mass failure, or any combination of the three (Dietrich and Dunne 1993). Hydraulic erosion results when a volume of water achieves a critical shear velocity. Thus, new channels may form during a discrete precipitation or melt event that adds excess water to a particular slope, when water accumulating in depressions is able to exceed the depression lip, or when terrain steepening provides excess power to existing runoff. By contrast, seepage can occur where sharp breaks in the terrain surface or springs lead to intersection with water tables. Otherwise, stable slopes and channel banks can be weakened by freeze-thaw action, leading to rapid extension of gullies without substantive overland flow. Mass failure (e.g., landslides) can occur following alterations to slope stability due to changes in the water budget from weather events, climatic shifts, forest fires, or human activity. Given the diverse mechanisms of channel formation, it is little wonder that most mapping approaches have focused on selected types of channel formation (i.e., hydraulic erosion) and the process that sustain them.

Process-based methods

Initially developed with coarse (>30 m) resolution terrain models, process-based predictions are derived from accumulations of upslope drainage area where minimum values of contributing area or “critical support area thresholds” that accommodate channels are directly analogous to Horton’s constant of channel maintenance (Horton 1932, 1945). Process-based methods are so-called because they do not delineate streams, but instead represent the *process* of water flow across the terrain surface; stream channels are inferred once sufficient water accrues from upslope drainage area. These procedures involve developing a directed flow field from interpretation of terrain surfaces (i.e., a *flow direction* surface; O'Callaghan and Mark 1984). The flow field is an implicit representation of a flow network, from which cumulative estimates of upslope drainage area (i.e., a *flow accumulation* surface) or specific catchment area (SCA; upslope contributing area per unit contour length; Wilson and Gallant 2000) are developed. Under steady-state assumptions, thresholds of SCA are used to estimate Horton’s constant with a critical support area threshold, and gridded stream maps are developed from SCA values above this threshold (e.g., Band 1986; Maidment 2002).

Critical support area thresholds are the most widely used approach for delineating stream networks due to well-developed procedures and many software packages that automate their implementation (e.g., ArcGIS, ESRI 2011; ArcHydro, Maidment 2002; TauDEM, Tarboton and Mohammed 2013). The resulting maps are visually appealing because they produce a clean dendritic aesthetic. However, there are several well-described shortcomings of this approach that challenge its utility in serious mapping applications (Band 1986; Tarboton and Baker 2008). Importantly, such approaches conflate two distinct steps in stream delineation: flow tracing and channel initiation

(Jasiewicz and Metz 2011). Flow tracing follows the path of steepest descent to mimic idealized behavior of water in a flow field, whereas channel initiation involves additional inputs such as critical support area thresholds or channel head maps. Although constant support area thresholds are excellent at flow tracing, they typically underperform at identifying channel heads. Further, in the absence of additional information regarding channel head locations, the *entire terrain surface* must be processed in order to map channels.

Interpretation of water movement over terrain requires a flow direction algorithm to route water across terrain surfaces, yet this is not always a straightforward process with LiDAR DEMs. The choice of algorithm (e.g., D8, D-infinity, or MD-infinity) can substantially alter estimates of SCA, especially for headwaters (Tarboton 1997; Seibert and McGlynn 2007). Moreover, their accuracy has also been found to be dependent on the resolution of digital terrain models (Zhang and Montgomery 1994; Wilson and Gallant 2000; Tarolli and Tarboton 2006). Further, internal drainage or errors in the terrain model may hamper completion of the flow field, thus several approaches for *filling*, *breaching, stream burning* and *DEM reconditioning* to enforce drainage through sinks and dam-like features have been proposed and are in widespread use (e.g., Saunders 1999; Soille 2004; Tarboton and Baker 2008). These approaches resolve indeterminate flow directions by modifying the DEM to allow drainage, but may do so at the expense of accurate and realistic representation of flow patterns (Baker et al. 2006). Most importantly, critical support area thresholds do not actually use the topographic detail in LiDAR DEMs to map channel heads, instead channel initiation is estimated statistically from existing maps or field observations (Baker et al. 2007; Julian et al. 2013). Thus, critical support area thresholds have been widely criticized as a "one-size fits all" approach for mapping channel initiation points, with the potential for gross errors of omission and commission (e.g., Montgomery and Dietrich 1988; Baker et al. 2007; Luo and Stepinski 2008; Elmore et al. 2013). Specifically, although SCA estimates the relative accumulation of water in a local terrain, it relates nothing about specific climatic or edaphic factors that govern the local water balance or the terrain properties that drive water velocities and erosive forces.

An important variant on the simple concept of upslope drainage is the *slope-dependent* critical support area (e.g., Montgomery and Dietrich 1988, 1992; Dietrich et al. 1993). Including local slope in predicting channel features is entirely reasonable because slope (S) and SCA are first-order factors that determine the erosive power of water (Montgomery and Dietrich 1988). Moreover, in humid soil-mantled landscapes, their joint distributions delimit *process domains* within watersheds (Montgomery and Dietrich 1994). Process domains are areas of relative equilibrium among driving (e.g., water accumulation implied by SCA and S) and resisting (e.g., vegetation cover and soil erodability) forces (Schumm 1979). Hence, interpretation of S and SCA may delineate domains dominated by distinct mechanisms including diffusive erosion (e.g., rain splash erosion that forms convex topography) or confluent erosion that leads to channelization (Montgomery and Foufoula-Georgiou 1993; Montgomery and Dietrich 1994). When geomorphic thresholds are exceeded due to modifications of either driving or resisting forces, major changes in form occur as landscapes adjust to new equilibria (Schumm 1979; Poesen et al. 2003). Channel heads, in particular, are landscape features that reside at or near geomorphic thresholds at the transition between unchanneled and channeled valleys in natural landscapes, marking regions initiated and maintained by concentrated runoff that produces sufficient shear stress to erode particles (Begin and Schumm 1979; Patton and Schumm 1975). Therefore, channel heads represent the boundary between two distinct process domains.

Several different procedures have been proposed related to the use of S and SCA to identify thresholds of channel initiation. The earliest procedures describe breakpoints in trends between S and SCA revealed among terrain pixels binned across log SCA (Montgomery and Dietrich 1988; Montgomery and Foufoula-Georgiou 1993; Ijjasz-Vasquez and Bras 1995; Tucker and Bras 1998; Stock and Dietrich

2003). Such comparisons often reveal initial increases in S with increasing SCA associated with convex terrain near watershed boundaries. As SCA increases, S decreases rapidly as hillsides become concave, then less so with unchannelized valleys and channels. Qualitative interpretation was initially used to distinguish different process domains, but subsequent investigators have proposed various quantitative methods to determine breakpoints (McNamara et al. 2006). In addition, S-SCA products (i.e., ~S*SCA; power index) and reciprocals (i.e., ~SCA/S; topographic wetness index; Beven and Kirkby 1979) of local slope and SCA have been proposed as alternative indices for mapping streams (Wilson and Gallant 2000).

The strength of process-based procedures is that they utilize the full distribution of topography and its arrangement to identify values of likely geomorphic thresholds in a manner consistent with theoretical mechanisms. The weakness of process-based procedures is that they do not represent all of the relevant mechanisms of channel initiation as much as their first-order drivers (i.e., water accumulation, slope). Further, such approaches do not include mitigating factors which can greatly alter those mechanisms and lead to errors of omission or commission in resulting maps, often associated with human activity (Heine et al. 2004; McNamara et al. 2006; Elmore et al. 2013). Recent models derived from these and similar approaches along the Atlantic coast of the US suggest that, although theoretically appealing and highly appropriate for certain landscapes, catchment-scale prediction of stream channels tends to underperform across heterogeneous physiographic and land use contexts (Heine et al. 2004; Baker et al. 2007; and Elmore et al. 2013). Process-based approaches assume the terrain is in pseudo-equilibrium with climate and extant land cover, thus their products are often a reasonable estimate of the landscape as it "should be" according to theory, rather than what actually exists. Work in developing countries or under scenarios of changing land cover (McNamara et al. 2006, Bezerra et al. *In review*) suggest that S-SCA thresholds are not indicative of existing channel head locations. Further, historical modification of landscapes can leave geomorphic legacies that disrupt empirical linkages between process-based theory and field observations, even when process-based mechanisms remain in operation (Smith and Wilcock 2015).

Direct-detection methods

As improvements in DEM resolution have become widely available, efforts at stream mapping have shifted from theoretical depictions of key processes to direct-detection techniques. This shift in focus emerged in response to substantial errors observed in process-based models or when natural processes could not be presumed (i.e., on Mars), and are largely based on interpretation of aerial imagery or local elevation derivatives such as curvature thresholds for mapping channel networks (Howard 1994; Wilson and Gallant 2000; Tarboton and Ames 2001; Molloy and Stepinski 2007). Early detection methods used local terrain to identify channel heads by comparing elevations within blocks of four pixels (Peuker and Douglas 1975) linked by accumulation over a flow field (Band 1986; Tarboton and Ames 2001). More recent efforts have focused instead on estimates of terrain curvature calculated across blocks of eight neighbors of a focal cell, specifically planform or tangential curvature (perpendicular to the slope direction), for distinguishing upwardly concave hillslopes and areas of convergent flow (Luo and Stepinksi 2006, 2008; Molloy and Stepinski 2007; Passalacqua et al. 2010). Such approaches rely on empirical estimates of terrain curvature independent of catchment conditions to identify hollows and depressions that, when they occur as groups of pixels in long, linear features, are a necessary (but not sufficient) property of mapped stream channels.

A fundamental but often overlooked advance in terrain analysis emerged from the quantification of multi-scale measures of terrain curvature termed *topographic openness* (Yokoyama et al. 2002). Measures of openness were developed as the maximum slope angle between a focal point and other peaks (positive openness; ϕ) or depressions (negative openness; ψ) defined at variable length

scales across the landscape surface. Positive openness may be understood as an analysis of line-of-sight from each pixel in eight different directions over a bare earth surface. The relative elevation and horizontal distance of each of the eight points that constrain their respective lines-of-sight describe eight maximum slope angles, which are then averaged. Negative openness is the same concept measured from below, rather than above, the terrain surface. Sofia et al. (2011) integrated measures of both topographic openness and curvature in predictions of stream channels in the Italian Alps, whereas Jones (2013) and Jones et al. (2014) found that simple thresholds of negative openness (i.e., ψ) resulted in reasonably accurate measures of channel head locations for several watersheds within the Maryland Piedmont using multi-temporal LiDAR.

An important advantage of direct-detection over process-based approaches is that they provide evidence of a channel-like morphology regardless of their position relative to upstream catchments. In other words, direct-detection provides an estimate of "what is" rather than "what should be". Impractical in coarser representations of terrain, such interpretation has become possible with datasets developed from aerial LiDAR. Availability of high-resolution (<2 m) terrain information makes detection of valley bottoms and stream channels far more precise in many landscapes (Heine et al. 2004; Tarolli and Dalla-Fontana 2009), but can be limited in narrow valleys with dense vegetative cover (James et al. 2007). The challenge for direct-detection lies in developing objective identification and mapping processes that extend across broad areas and adapt to different terrain or land use contexts.

A second important limitation of direct-detection from elevation derivatives such as slope or curvature is that, because they are calculated from the values of the eight adjacent pixels, their performance is directly related to the resolution and the point density of the underlying terrain model (e.g., Wilson and Gallant 2000; James et al. 2007; Tarolli and Dalla Fontana 2009). Research has suggested that the value of curvature in detecting channel heads can be scale dependent, and that critical scales of curvature necessary for channel head formation can vary with different landscape contexts (Lashermes et al. 2007; Pirotti and Tarolli 2010). Lashermes et al. (2007) suggest that threshold measures of curvature for identifying channels are likely to generate errors unless first examined for region-specific power law behavior. That is, the authors advocate for analysis of nonlinear breaks in the log-log relationship of terrain curvature values and pixel resolution to identify the most appropriate scale for detecting channel heads in each region of interest. However, apart from being a computationally intensive exercise, this assertion continues to presume relative homogeneity in channel generating processes and underscores an inherent shortcoming of local measures. By contrast, openness measures are generated from a terrain analysis that is inherently multi-scale, thus openness algorithms offer a relatively straightforward opportunity to automatically adapt to local terrain and land use conditions.

Geomorphons

As an application of openness in terrain classification, geomorphons are scale- and orientation-independent geomorphic features that constitute bare-earth terrain (Jasiewicz and Stepinski 2013). Geomorphons can be processed from DEMs through an extension (*r.geomorphon*) to the free and open-source GRASS GIS platform (GRASS Development Team 2017). Geomorphons assess elevations along lines-of-sight in eight directions surrounding each pixel of the study area, out to a user-specified search distance. A different landform type is assigned based on the observed ternary pattern of higher, lower, or equal elevations surrounding the focal pixel, as depicted in Figure 1 below.

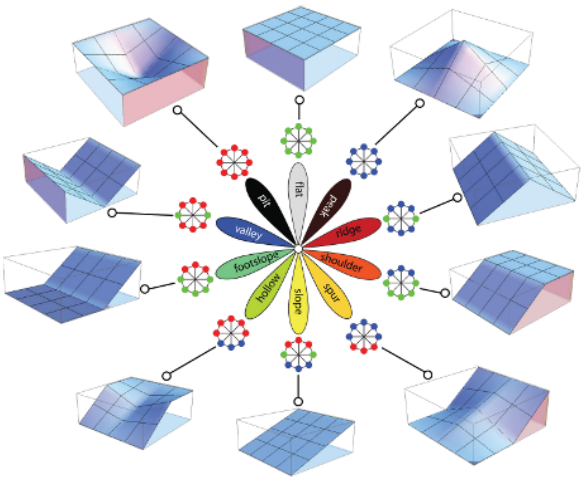

+	0	1	2	3	4	5	6	7	8
0	FL	FL	FL	FS	FS	VL	VL	VL	PT
1	FL	FL	FS	FS	FS	VL	VL	VL	—
2	FL	SH	SL	SL	HL	HL	VL	—	—
3	SH	SH	SL	SL	SL	HL	—	—	—
4	SH	SH	SP	SL	SL	—	—	—	—
5	RI	RI	SP	SP	—	—	—	—	—
6	RI	RI	RI	—	—	—	—	—	—
7	RI	RI	—	—	—	—	—	—	—
8	PK	—	—	—	—	—	—	—	—

Figure 1: Forms represented by geomorphons (left). Lookup table used to aggregate geomorphons into common forms (right). Source: https://grass.osgeo.org/grass74/manuals/addons/r.geomorphon.html

There are precisely 498 unique patterns identified by the ternary approach. Of these 498 theoretical landforms, the 30 most common types account for 85% of all cells and this group can be further reduced to 10 most recognizable landforms using the lookup table in Figure 1. These landforms are: flat (FL), peak (PK), ridge (RI), shoulder (SH), spur (SP), slope (SL), hollow (HL), footslope (FS), valley (VL), and pit (PT). A sample of a landscape classified using geomorphons is illustrated in Figure 2.

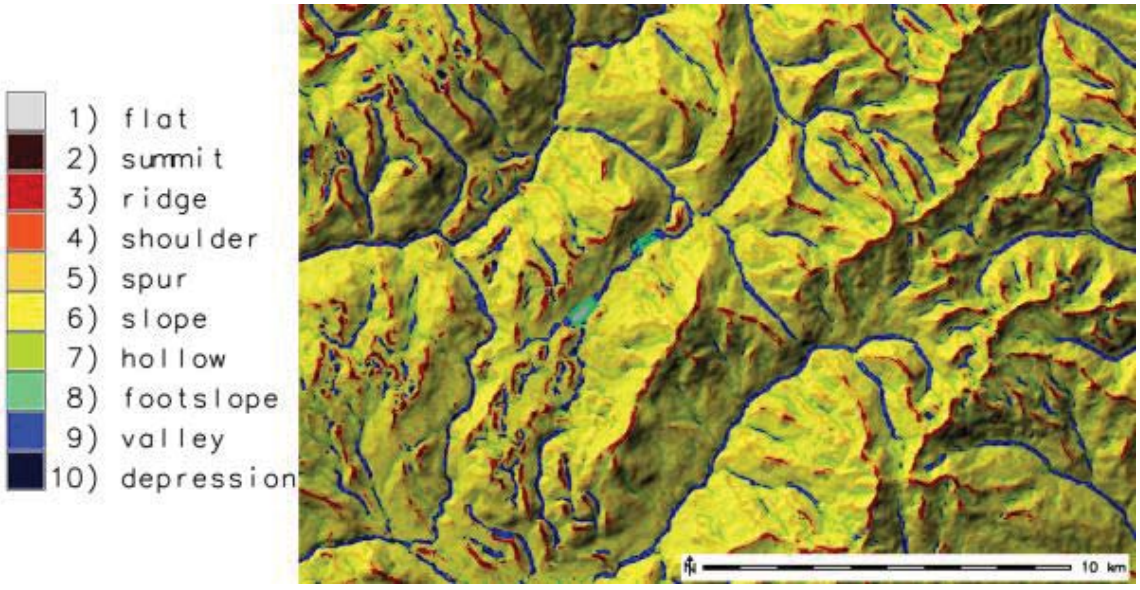

Figure 2: Example of geomorphon results. Source: https://grass.osgeo.org/grass74/manuals/addons/r.geomorphon.html

The scale of geomorphons is flexible and automatically adapts to differing terrain. This adaptation occurs because features are classified based on line-of-sight criteria instead of differential geometry within a fixed window as in other direct-detection methods (e.g., curvature; Passalacqua et al. 2010). Line-of-sight analysis is constrained by a user-specified search distance that determines the maximum extent over which features can be identified. With a larger search distance, features can be identified across broader extents. However, landform classifications quickly converge over increasing search distances, as the line-of-sight approach adapts to local terrain. See Figure 3 below for an example:

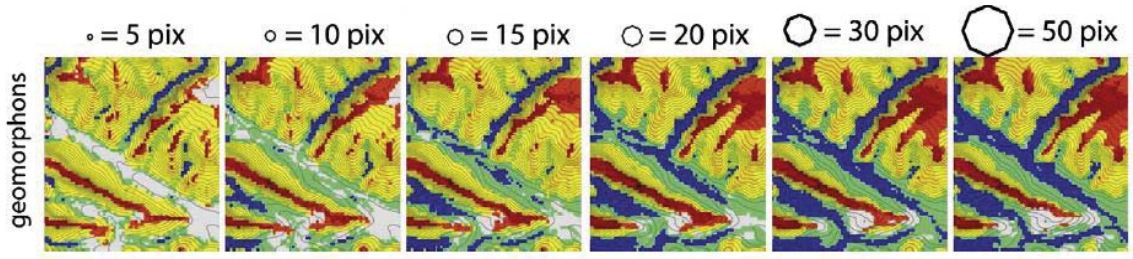

Figure 3: Terrain features classified by geomorphon converge as search distance is increased. There is minimal difference between the map produced with 20-pixel search radius and the ones produced with 30- or 50-pixel search radii on a 30-meter DEM. Source: Jasiewicz and Stepinski, 2013.

The flexible, self-adapting property of geomorphons is both desirable and exploitable for stream channel mapping. It allows rapid identification of broad stream valleys without the need for multiple search distances, thus improving computational efficiency. Intentionally small search distances can also be used to isolate and identify local-scale features such as channel-like depressions. In this case, the search distance is restricted to be smaller than the width of the surrounding valley, so the geomorphon algorithm is unable to perceive valley topography. Instead, it detects local depressions as valley, pit, or hollow features and delineates them as such, when in reality they are channels within a broader valley feature. The application of geomorphons at both the "valley-extent" and "channel-extent" is described in more detail in the methods below.

When it comes to detecting channel-like depressions, we expect geomorphons to be superior to both terrain curvature and topographic openness as a direct-detection method for the following reasons. Both geomorphons and openness rely on line-of-sight criteria that allow interpretation of terrain over variable extents. Thus, their ability to detect features broader than 3 pixels wide should be as good as, or superior to, curvature. We expect identification of smaller channels less than 3 pixels to be similar across all techniques, but that geomorphons and openness should produce more contiguous output than curvature across broader channels and along most channel lengths. Therefore, while we expect the headward extent of detection to be similar across all methods, we expect geomorphons and openness to produce fewer errors of omission than curvature in the overall detection of channel-like features and their contiguity.

We expect geomorphons to outperform openness in delineating channel features because geomorphons automatically integrate both positive and negative openness to provide more information about the terrain than either measure could provide independently. We will test this expectation by direct comparison, but also by developing predictions based on our own custom combination of positive and negative openness to more fully assess the results. By further interpreting the integrated openness information and classifying terrain into discrete features, geomorphons automatically distinguish local terrain signals associated with features such as footslopes that could otherwise be confused with, and misinterpreted as, channels by openness alone. Thus, we expect geomorphons to produce fewer errors of commission than openness. From a practical standpoint, the *r.geomorphon* algorithm offers greater

flexibility and control of the search radius inherent to openness and, at no additional computational cost, produces a number of outputs describing the terrain in addition to the ternary forms. Therefore, geomorphons represent value-added over the openness technique alone.

Cartographic and geomorphic elimination

A relevant limitation of all direct-detection methods is that, because they are developed from local topography, they can produce noisy output due to inherent error in LiDAR data or imprecise detection criteria. Sofia et al. (2011) recommended integrating noise into estimates of channel prediction uncertainty. Noise reveals itself as many small depressions of just one or a few pixels in size, but it can also produce spurious errors in resulting stream maps or, conversely, can reduce the functional connectivity of resulting channel networks. As a result, several authors (Passalacqua et al. 2010; Pelletier 2013) advocate for noise elimination through DEM filtering or denoising. Denoising is an image processing technique derived from signal processing theory that has the advantage of removing spurious elevation values without degrading underlying signal (e.g., edges) in the original input (Sun et al. 2007). Yet even after denoising, many channel mapping protocols that rely on direct-detection utilize areal thresholds to further eliminate small, isolated depressions that are unlikely to be part of a channel system (Passalacqua et al. 2010; Sofia et al. 2011; Passalacqua et al. 2012; Sangireddy et al. 2016, Hooshyar et al. 2016). Passalacqua et al. (2010) originally coined the resulting patches of channel-like depressions above such threshold values a “skeleton”. Because such areal thresholds have no basis in geomorphic theory but are recommended solely to enhance analytical integrity, we term such elimination as “cartographic”.

By contrast, other authors advocate for elimination of spurious channel-like depressions based on geomorphic principles. After all, channels represent a specific form of process domain typically associated with valleys (Montgomery and Dietrich 1994). Sofia et al. (2011) took a probabilistic approach, requiring cumulative agreement among skeletons derived from curvature as well as openness. Jasiewicz and Metz (2011) advocated for using valleys to isolate channel skeletons, whereas Hooshyar et al. (2016) attempt to isolate both valley and channel skeletons. In each case, the authors used the geomorphic context of a depression as justification for inclusion in or elimination from the channel skeleton. The rationale for geomorphic elimination is that valleys are a logical place to find stream channels in natural terrain. We agree that geomorphic elimination represents a sound initial step to be preferred over cartographic elimination when possible, but caution that such techniques may not be sufficient for identifying all channels in human-modified terrain. In such contexts, channels may form as a result of concentrated runoff redirected by land development and skeletons may be fragmented by road crossings (Passalacqua et al. 2012). Thus, elimination of spurious channel-like features needs to be able to identify channels occurring in appropriate geomorphic contexts *and* those originating from anthropogenic sources while eliminating spurious features.

Methods

This section details the steps taken to develop stream channel maps for the 14 study watersheds. First, we describe the methods used to carry out the field assessments at the study sites, then we describe our empirical evaluation of direct-detection channel maps including: processing elevation data; generating calculations of curvature, openness, and geomorphons; manipulating these layers to delineate channel skeletons; and assessing their performance relative to field observations. Next, we develop linear stream networks from geomorphon channel skeletons and consider methods for determining channel width and bank height. Lastly, we discuss the estimation of flow permanence. An overview of these steps is presented in Figure 4.

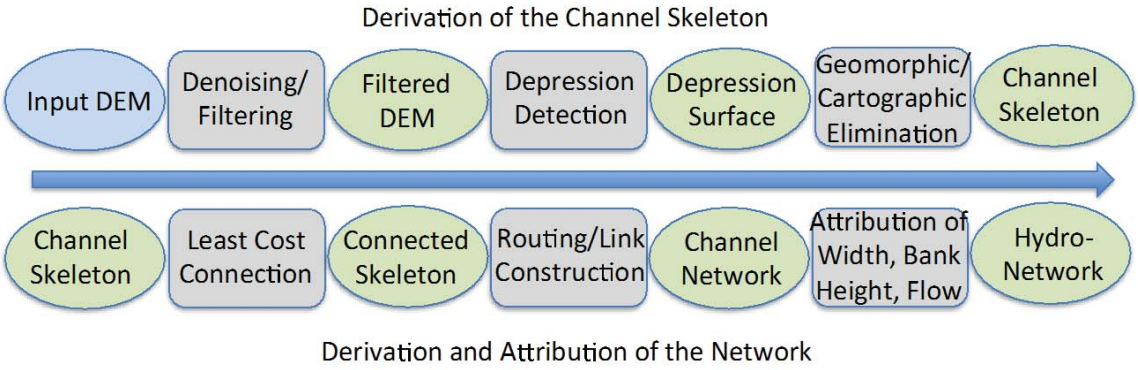

Figure 4: Overview of channel mapping workflow. Input data are shown in blue ovals, processes are shown in gray rectangles, and data products are shown in green ovals.

Fieldwork

To assess the performance of geomorphons and other methods at accurately mapping channel features, the project team visited 14 field sites around the Chesapeake Bay watershed in the spring and summer of 2017. In addition to collecting data on the location of channel heads and their flow status, the purpose of the field visits was to provide on-the-ground context and field-verification of features observed through GIS mapping efforts. Fieldwork enabled the project team to interpret terrain data and its derivatives with first-hand knowledge of the conditions on the ground at the study watersheds. This was valuable as some features that appear as errors in a GIS environment, such as disconnected streams or valleys, are in fact real features when observed through field visits.

Field sites were selected such that the field crew visited each of the physiographic provinces in the Bay watershed and, where possible, at least two distinct land use contexts in each province (Figure 5). These land uses included forested, developed, and agricultural. Selecting field sites in this way allowed the field crew to assess the influence of physiography and its interaction with land use on channel initiation and algorithm performance.

Prior to each field visit, the field crew assessed LiDAR elevation data and derivatives to inform the visit. Based on this assessment, likely channelized valleys were identified and headward extents were predicted from visual interpretation of hillshades. At each field visit, typically starting from the downstream end of the study watershed, the field crew walked upstream to areas of interest previously identified. The positional location of channel features like flowing water, occurrence of channel heads, locations of active erosion and channel incision, as well as any channel discontinuities were recorded. All features were photographed using a geotagging-enabled smartphone so that their locations could be imported in a GIS environment and used to assess stream mapping methods.

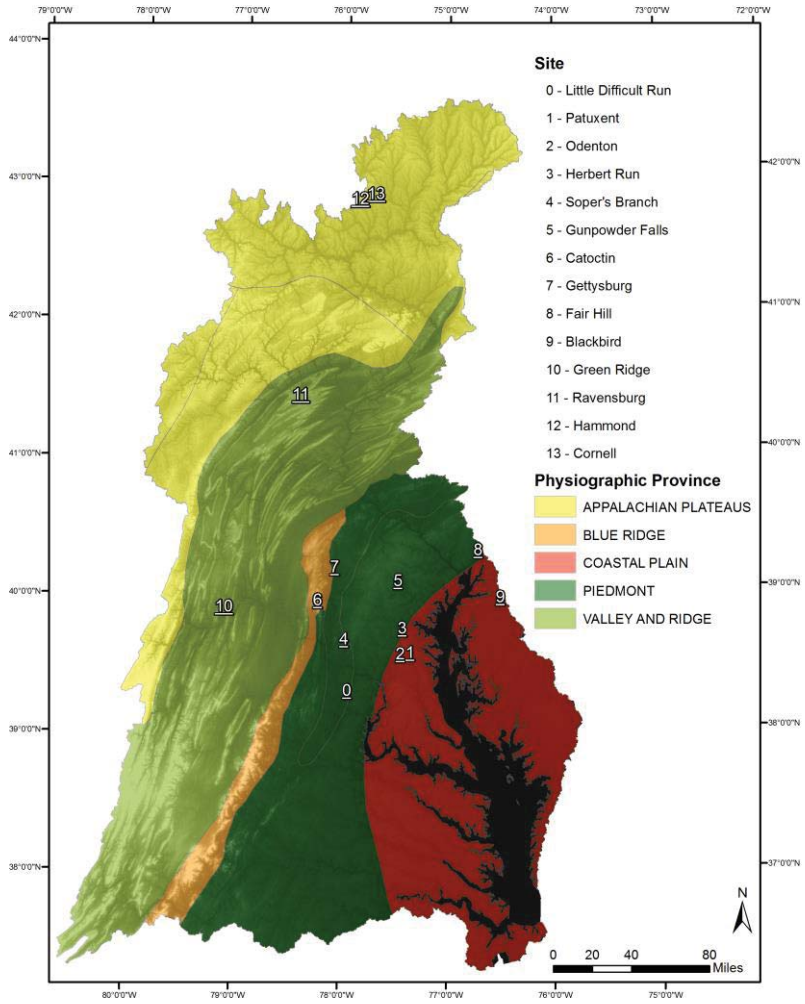

Figure 5: Map showing location of field sites across Chesapeake Bay watershed with physiographic province information overlaid.

Processing elevation data

Elevation data were crucial to the delineation of stream networks. Several sources of elevation data were used in this project including digital elevation models (DEMs) created from various LiDAR collections and the seamless, 10-meter resolution National Elevation Dataset (NED), available from the U.S. Geological Survey (Gesch et al. 2002). The NED was used to identify valleys at a broad extent, a task that does not necessarily require the level of detail in LiDAR DEMs, while the LiDAR DEMs were used to delineate channels at a local extent within the valleys.

To remove noise and allow for cleaner and more contiguous feature identification, LiDAR elevation data are often denoised or smoothed using a feature-preserving filter (Passalacqua et al. 2010, Lashermes 2007). We pre-processed LiDAR DEMs using a mesh-denoising filter (Sun et al. 2007; implemented in SAGA GIS, Conrad et al. 2015) prior to using them as input to calculations of geomorphons, curvature, or openness. Mesh denoising of LiDAR DEMs removes irregularities in a surface while preserving features and edges. Similarly, the 10-meter NED was smoothed to allow better identification of broad stream valleys using geomorphons. While the coarser resolution NED inherently

eliminates much of the noise found in high-resolution LiDAR data, larger anthropogenic features such as bridges may still be present and cause undesired interruptions to stream valleys. A Gaussian filter was applied to generalize the terrain and reduce the distinct signal from roadways and similar anthropogenic features.

Detecting channel-like depressions

Based on the literature review above, it was clear that local terrain curvature remains the default method for detecting depressions in modern mapping methods. Topographic openness has been suggested as well, but it was unclear how to best identify channel-like features using its output maps. However, a generalized method is critical for automated mapping because it allows for objective processes to be performed across all land use and physiographic contexts. Following the suggestion of Lashermes et al. (2007), we performed a threshold analysis on terrain curvature (default curvature output calculated using the *Curvature* tool in ArcGIS Spatial Analyst toolbox), and negative and positive openness (calculated using the *Topographic Openness* tool in SAGA GIS using a search radius of 10 meters) rasters to isolate channel-like depressions of interest for each of our study sites. To identify these thresholds, QQ normal plots were analyzed for inflection points that distinguished extremes from the majority of values (see Appendix A). Pixels in the curvature and openness rasters exceeding these thresholds were retained as depressions of interest. A unique combination of positive and negative openness was used to create a depression map more directly comparable to geomorphons. This map was created by first isolating threshold positive openness pixels that were contiguous with pixels of 0.75 acres contributing area or greater, then isolating threshold negative openness pixels contiguous with the previous isolation.

Geomorphons were calculated using the *r.geomorphon* extension of the free and open source GRASS GIS 7.2.2 on Windows 7. *r.geomorphon* has five required user-input parameters that can be customized to produce a landform classification map tailored to the user's needs. The five required parameters are elevation, outer search radius, inner search radius, flatness threshold, and flatness distance. Several optional outputs provide additional information about the geometry and relative position of geomorphons in the surrounding terrain. To detect channel-like features using geomorphons, the outer search radius was set to a relatively small distance of 10 meters in order to constrain the line-of-sight analysis to the terrain immediately surrounding the focal cell. An inner search radius was not specified so that pixels immediately adjacent to the focal cell were included in the analysis. By using this combination of search radii with a detailed LiDAR DEM, channel banks were interpreted as valley walls, thus channel-like depressions were classified as valleys or pits (Figure 6).

For most study sites, it was not possible to directly compare threshold values of curvature, openness, and classified geomorphon rasters with field observations without first eliminating some of the pixels identified in each map. Curvature and openness maps in particular often exhibited many pixels or groups of pixels above threshold values that were clearly not part of the stream network, but would nonetheless need to be considered in an automated method. Thus, we decided to focus our comparison of methods on the *channel skeletons* that result from further processing and elimination of noise from initial depression maps.

Constructing channel skeletons

According to Sangireddy et al. (2016), their method relies on accumulation of threshold pixels over a flow field to perform an initial elimination of spurious depressions. The approach is based on the geomorphic conceptualization of channel heads occurring on the lower portion of hillslopes with somewhat larger contributing areas than divides. Passalacqua and Foufoula-Georgiou (2015) provide some suggestions for how to determine the accumulation value from ½ the median hillslope length within a region. We applied a moderate contributing area threshold of 0.75 acres (Passalacqua et al.

2010) to maps of curvature, positive openness, negative openness, and geomorphons as an initial form of geomorphic elimination.

For geomorphon maps, we followed the suggestions of Jasiewicz and Metz (2011) and Hooshyar et al. (2016) and used delineation of river valleys as a separate initial geomorphic elimination of spurious depressions. To delineate river valleys, we first employed the Gaussian filtered 10-meter NED as the input elevation grid to *r.geomorphon*. The outer search radius, which constrained the line-of-sight analysis, was set to 200 meters – a distance sufficiently large to encompass headwater stream valleys. An inner search radius, also referred to as a "skip" radius, was also specified. This parameter further constrains the line-of-sight analysis such that any pixels between the focal cell and the skip radius are not considered in the calculation of geomorphons. We specified a 20-meter skip radius to prevent channels and other local irregularities from interrupting the line-of-sight and allow better detection of broader features like valley walls (Figure 6). These settings were used to generate a classified map of geomorphons at the "valley-extent" for the entire Chesapeake Bay watershed

To better distinguish features in the valley-extent geomorphon map that were associated with stream valleys, we focused on convergent features that were clearly connected to larger order fluvial systems. The connected valley network thus consisted of all pit, valley, and hollow[1] geomorphons from the valley-extent geomorphon map that were contiguous with a rasterized version of the NHDPlus High Resoultion (NHDPlus HR) stream network (U.S. Geological Survey 2017). Valley contiguity was defined as all pit, valley, and hollow cells directly overlapping with the NHDPlus HR or connected to it through other pit, valley, and hollow cells. We used the resulting connected valley network as a geomorphic filter to eliminate channel-like depressions identified by geomorphons at the channel extent that were not contained by or contiguous with the valley network.

Following geomorphic elimination of spurious depressions by either flow accumulation or contiguity with a valley network, we employed a cartographic elimination on the remaining depressions identified by all methods. Here our goal was to remove small groups of spurious pixels erroneously identified as channels. We used the *Region Group* operation in ArcGIS to calculate the number of pixels belonging to each discrete group of depressions remaining after geomorphic elimination. A histogram of the size distribution was created where the first bin contained a disproportionately large number of very small depressions. This bin was used as an areal threshold for elimination of small, isolated clusters of pixels likely to be noise (Passalacqua et al. 2010). The remaining pixels formed the *channel skeletons* for each detection method that were compared relative to field observations.

Comparing detection methods

With channel skeletons developed by applying various elimination techniques to channel-like depressions identified using curvature, openness, or geomorphons, we assessed their relative performance in predicting channel head locations. This was accomplished by measuring the distance along a flow line between the headward extent of the channel skeletons and channel heads observed during field visits. Positive distances indicated commission in the detection method (i.e. predicted channel head was upslope of observed head), whereas negative distances indicated omission in the detection method (predicted channel head was downslope of observed head). A distance of zero

[1] Hollows with a negative intensity were included. The sign and magnitude of the intensity value describe the degree to which the focal pixel is above (positive intensity) or below (negative intensity) the cells comprising its visibility neighborhood. Cells classified as hollow with a negative intensity are convergent, typically located at the headward extent of stream valleys or the junction of steep tributaries and a flatter valley, and thus were included in our valley network.

indicated an entirely accurate prediction by the detection method (predicted channel head and observed channel head coincide). The recorded distances were analyzed using statistical summaries including median, mean, standard deviation, root mean square error (RMSE), as well as graphical summaries such as box plots. Commission and omission frequencies were also analyzed. We tested for differences in among group variance using Levene's Test. Due to differences in sample sizes and variance across factors, we tested for significant differences among land uses and physiographic provinces using a non-parametric Kruskall-Wallis procedure.

The goal of this comparison was to better understand the relative costs and benefits of using various automated procedures in different land use and physiographic contexts; not necessarily to establish one approach as superior to another in minimizing distance to the observed heads. Indeed, as far as direct-detection methods were concerned, our initial expectation was that all approaches would be relatively similar. However, we were particularly concerned by the potential for large or frequent errors of commission (i.e., predicting a channel that did not truly exist) and less concerned with errors of omission because some omission is an accepted feature of current national maps (i.e., NHD maps produced at 1:100,000 scale will inherently have fewer streams than those at 1:24,000 scale). A secondary goal was to examine the relative impacts of the geomorphic and cartographic elimination procedures on depression maps. Further, we wanted to understand whether there was differential impact associated with factors such as land use, physiography, or detection method. We accomplished this by analyzing pixel counts of depression maps from all methods before and after geomorphic and cartographic elimination.

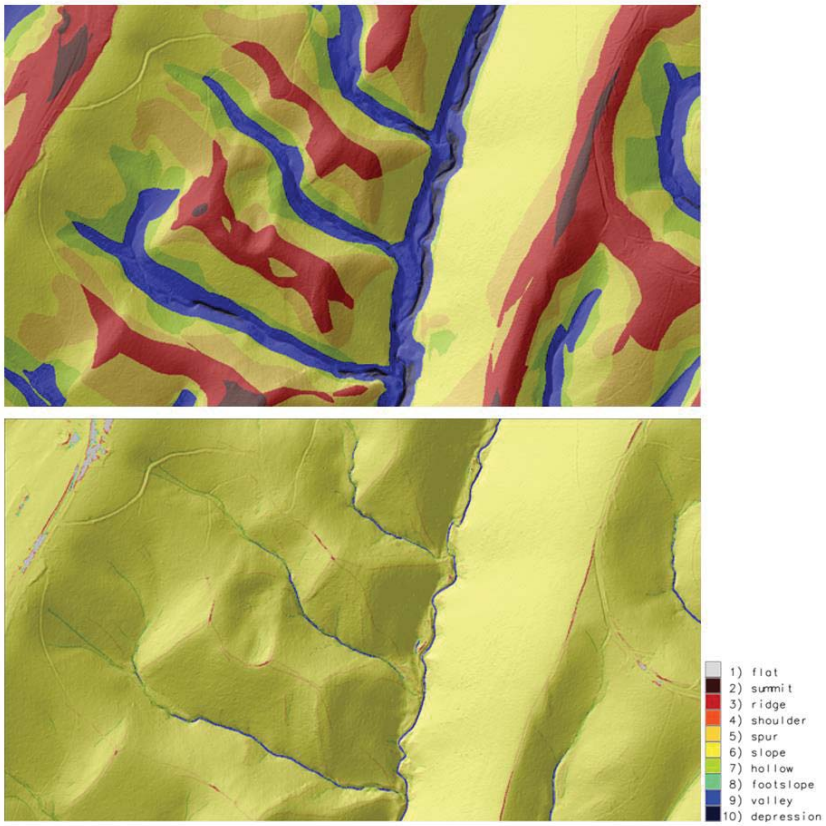

Figure 6: Geomorphons calculated in the same location at the valley extent (top) and channel extent (bottom). Note that the search parameters have a substantial impact on the resulting landform classification map.

Constructing the channel network

While the two-dimensional channel skeleton delineated using geomorphons can be a useful product for applications concerning edge-of-stream zones and channel discontinuities, other applications require a connected linear stream network, akin to traditional hydrographic maps. This type of network can be constructed using the geomorphon channel skeleton and a cost surface to perform a cost connectivity analysis. The cost surface incorporates the channel skeleton and other convergent features in the geomorphon map with elevation values from the DEM to give preference to paths following convergent features at lower elevations, and to penalize other features. When creating the cost surface and using it to connect channel features, the DEM can be constrained to the extent of the broader valley network to eliminate unnecessary processing of the entire terrain surface. Pixels in the cost surface coinciding with the channel skeleton were assigned a cost equal to the DEM elevation for the pixel; pixels in the cost surface not belonging to the channel skeleton but classified as hollows in the geomorphon map were assigned a cost equal to 5x the DEM elevation at the pixel; all other pixels in the cost surface were assigned a cost equal to 100x the DEM elevation. Creating the cost surface in this way encouraged the cost connectivity algorithm to connect regions of the channel skeleton along convergent features at low elevations, however, it also enables direct connections across roads or other convex features when a lower-cost path is not available.

The output line network from the cost connectivity analysis and the channel skeleton were then "burned" into the DEM, so that their elevations were ten units lower than the remainder of the terrain in the DEM. Sinks in this DEM were then filled and D8 flow directions were calculated. Using the flow direction surface, a weighted flow accumulation was performed using the channel skeleton as a weight raster. This operation accumulated only those pixels belonging to the channel skeleton, resulting in a raster where pixel values greater than zero begin at the very headward extent of the channels identified by geomorphons, and values increase in the downslope direction along the channel skeleton. A small threshold (e.g.; 20 pixels) was applied to remove values of zero and very short segments from the weighted accumulation raster, so that a linear stream grid could be obtained. This grid is analogous to the stream source grid used by TAUDEM (called "src" by default) and the stream grid used by ArcHydro (called "Str" by default) and can be used as input to ArcHydro/TauDEM tools to segment streams, convert streams to polylines, and assign network connectivity (i.e. add unique identifiers linking flow from one segment to the next downstream segment).

Shortly before the submission of this report, the project team began exploration of the GRASS GIS add-on *r.stream.extract* (Jasiewicz and Metz 2011), which can quickly and efficiently automate the process of stream tracing using a cost surface derived from a DEM, similar to the method described above. This add-on is capable of identifying stream initiation points via a flow accumulation search algorithm and tracing them downslope, but it can also trace streams from previously identified stream heads or fragments of stream routes identified through field or cartographic studies. We are currently exploring the potential to use the channel skeleton identified from geomorphons as input to *r.stream.extract* as a means to connect the skeleton into a linear network. Initial results are promising and exploration will continue in future work.

Estimating channel width and bank height

Development of a linear channel network represents a powerful and potentially useful framework for summarizing distributed estimates of channel width and bank height. Prior to summary, it is possible to use the channel skeleton itself to obtain estimates of both parameters. Using the area

outside the skeleton as a "source grid" and the skeleton as a "cost surface" in a *Cost Distance* function within ArcGIS, it is possible to map the distance from each stream bank within the region of pixels that constitute the channel. This distance surface decreases with proximity to each bank, reaching a maximum at or near the channel midpoint. With this distance surface as input to a circular *Focal Maximum* function with a radius of 10-20 meters, the largest width estimates (from channel bank to center) can be isolated and doubled to estimate the width (from bank to bank). Alternatively, it is possible to convert the channel skeleton raster into polygons and use them as input to the *Polygon to Centerline* tool in ArcGIS Pro. The resulting centerlines can be used to extract cost distance values along the channel skeleton that should be doubled to estimate channel width. Either way, results produce a distributed estimate of channel width that varies with physiographic constraints and may be aggregated or summarized across segments of the channel network.

Bank height estimates can be obtained from the integration of optional outputs from *r.geomorphon*. One output, called the *intensity* raster, describes the average elevation of the eight maxima or minima that constrain lines-of-sight across all eight transects for every focal pixel. For pit geomorphons, all eight transect constraints are higher than the focal pixel, so the value of the intensity raster is a relative estimate of surrounding high points (i.e., top of banks). For valley geomorphons, there can be 5, 6, or 7 transects higher than the focal pixel, and in each case the remaining transects may be equal or lower than the focal pixel (see classification table in Figure 1). A second optional output of *r.geomorphon* produces the ternary code for each geomorphon pixel. The ternary code specifies the relative elevation for each transect constraint (i.e., higher, lower, or equal). Using a custom look-up table developed by PI-Baker in a separate research effort, *intensity* values were converted to the average elevation of only those points higher than the focal pixel, as described by the ternary code. These values are used as an estimate of bank height. Empirical evaluation (outside the scope of this report) has suggested that this is often a *very* reasonable estimate, or precisely analogous to what would be obtained from a cross-section of the DEM. Bank height estimates are thus obtained for *every pixel in the channel skeleton*, or potentially hundreds to thousands of estimates in any particular stream reach. The Central Limit Theorem suggests that even large error in individual pixelate estimates will become vanishingly small across reaches and segments of the channel network, as summaries converge on the actual value.

Estimating flow permanence

We estimated flow permanence (perennial, intermittent, or ephemeral) by calculating regional low flow statistics and relating low flows to drainage area. First, we used the newly available Surface Water Toolbox created by the USGS (SWToolbox, Kiang et al. 2018) to estimate seven-day two-year low flows (7Q2) at stream gauges in and around our study areas. 7Q2 is defined as the lowest mean discharge over any seven consecutive days with a recurrence interval of 2 years. The toolbox enables estimates to be calculated on a month-to-month basis. To estimate flow permanence, we examined 7Q2 in January and July. These two months were chosen because in January we can expect low levels of evapotranspiration (ET), higher groundwater levels, and thus a higher 7Q2. In July, we can expect the opposite: high ET, low groundwater levels, and low 7Q2. Thus, if a stream's 7Q2 is functionally zero in January, we considered the stream to be ephemeral; if the 7Q2 is greater than zero in January but functionally zero in July, the stream was considered to be intermittent; if the 7Q2 is greater than zero in both January and July, we considered the stream perennial. Because the equations used to calculate 7Q2 rarely return zero, we accepted a 7Q2 of 0.1 cubic feet per second (cfs) to be functionally zero.

SWToolbox does not currently have the capability of estimating 7Q2 on ungauged streams and while this functionality is built into another USGS tool, StreamStats (Ries et al. 2017), StreamStats does not calculate low flow in all geographies and thus was unsuitable for our application. Because nearly all

of the streams in our study sites are ungauged, we used linear regression to relate drainage area to 7Q2 estimates at stream gauges surrounding our study sites, estimated using SWToolbox. We then used these relationships to determine the drainage area needed to support 0.1 cfs in January and July so stream reaches could be classified according to the criteria set forth in the previous paragraph. For example, if the regression determined that 0.75 square miles were needed to generate a 7Q2 of 0.1 cfs in January and 1.0 square miles (sq. mi.) were needed in July, sections of the stream network with a contributing area smaller than 0.75 sq. mi. would be classified as ephemeral, sections with contributing area between 0.75 and 1.0 sq. mi. would be classified as intermittent, and sections with contributing area greater than 1.0 sq. mi would be classified as perennial. For details on the regressions and drainage area thresholds for each site, see the results section below.

Results and Discussion

Processing DEMs

Mesh denoising removed some of the pixelate noise in LiDAR DEMs and the resulting curvature, openness, and geomorphon maps derived from them, without removing the topographic signal of features in the terrain. In geomorphon maps specifically, features identified using denoised DEMs were more contiguous and well defined (Figure 7). The improved contiguity of features had an impact on cartographic elimination of channel-like depressions, resulting in larger areal thresholds being identified and fewer spurious features meeting the criteria for inclusion in the final channel skeleton.

The Gaussian filtering of the 10-meter NED resulted in a smooth, generalized representation of the terrain surface that retained large, landscape-scale features such as stream valleys (Figure 8). The topographic signal from anthropogenic features including roads and bridges was largely removed. As a result, the valleys delineated using geomorphons at a broad extent were more contiguous.

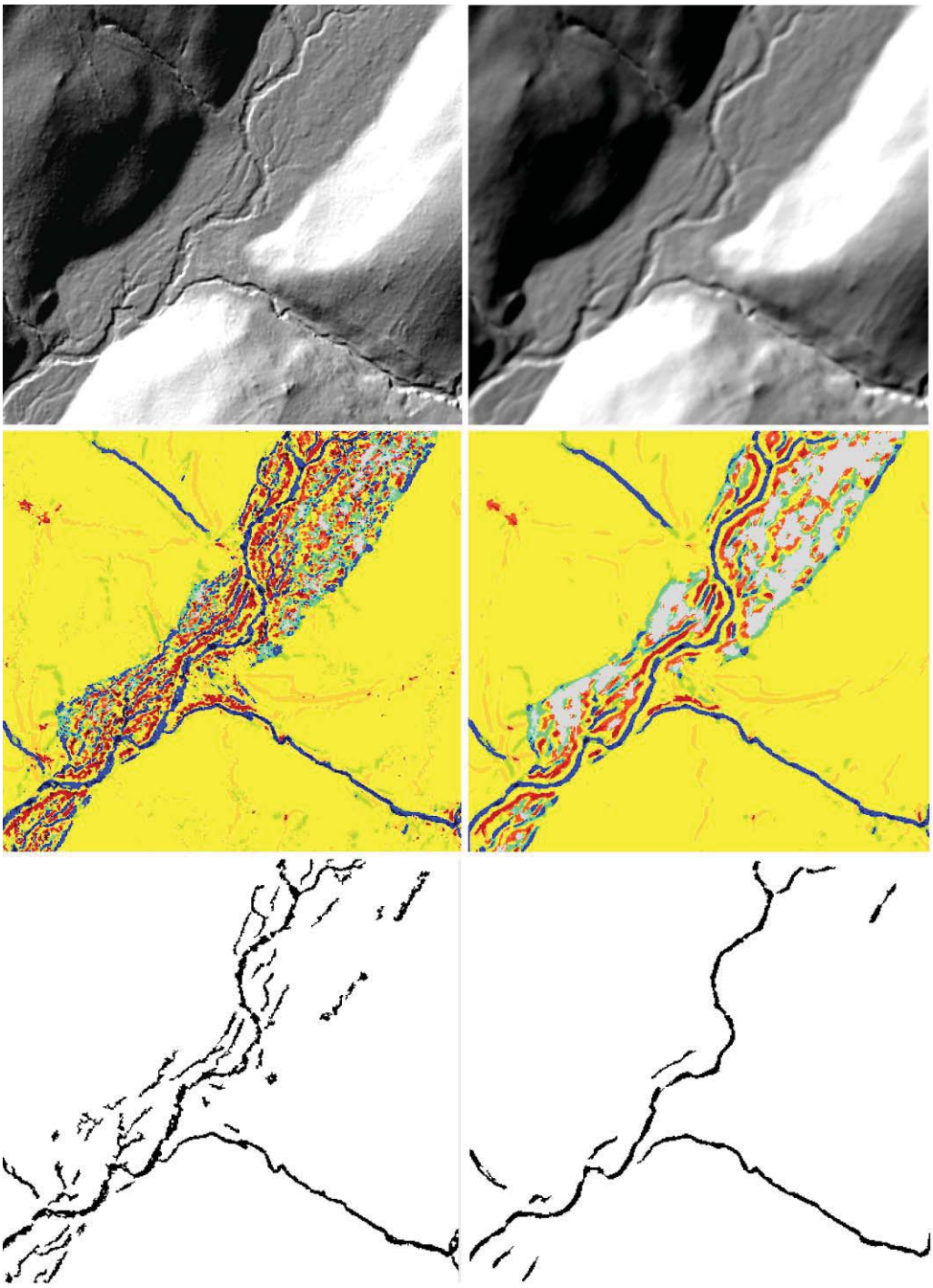

Figure 7: Comparison of hillshade (top), channel-extent geomorphons (middle), and channel skeleton (bottom) using unaltered LiDAR DEM (left column) and mesh denoised LiDAR DEM (right column). Geomorphons and channel skeleton derived using denoised DEM are less fragmented and more contiguous overall.

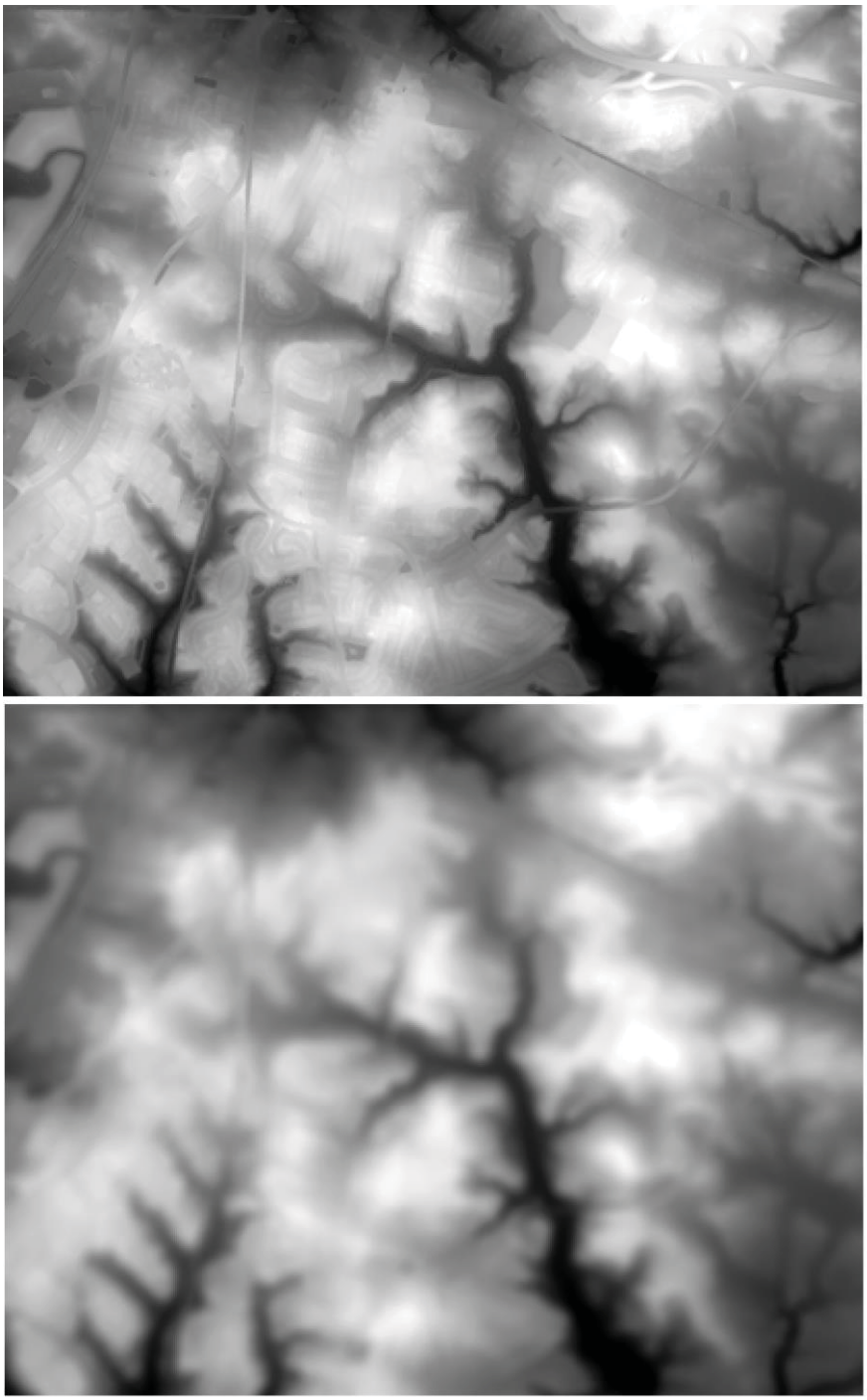

Figure 8: Comparison of unaltered 10-meter NED (top) and Gaussian smoothed NED (bottom). Several bridges that interrupt the stream valleys in the unaltered NED have been largely removed from the smoothed NED while still retaining the overall characteristics of the valleys and surrounding landscape.

Comparison of detection methods

Channel skeletons for depressions identified by curvature, negative openness, positive openness, and geomorphons were developed to assess their potential for automated application. Combined openness skeletons were also developed for direct comparison with geomorphon skeletons (which also integrate positive and negative openness). Two geomorphon skeletons were developed: one from the same accumulation-based thresholds as the others (i.e., channel-only geomorphon), and another using geomorphic elimination by valley extent (i.e., valley network geomorphon). We compared estimates of channel head location from each of these methods to locations identified and mapped from field visits. The field observations were not an exhaustive inventory, but rather a representative set selected across each study site based on land use, physiography, and accessibility. For each method, we assessed the distance between each observed channel head and the closest headward extent of each channel skeleton (Figure 9).

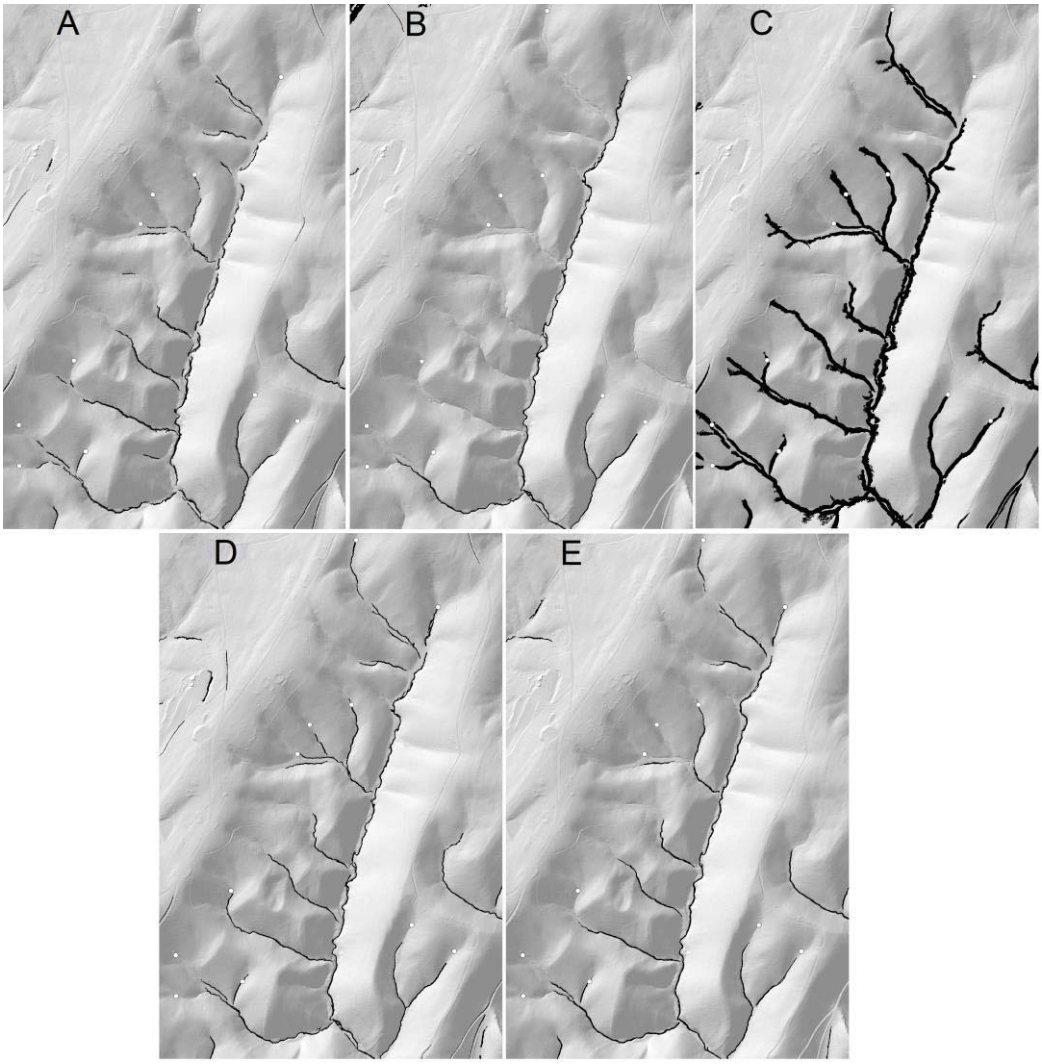

Figure 9: Comparison of channel skeletons delineated using (A) curvature, (B) negative openness, (C) positive openness, (D) openness combination, and (E) geomorphons (geomorphic elimination by valley extent). White points represent observed channel heads. Although the methods generally performed similarly, marked local examples of commission were often noted for positive openness (C) and greater omission was observed for negative openness (B). Overall, combined openness and geomorphons appeared marginally more effective and contiguous than curvature, as expected.

Distances between channel heads at each site and those predicted by channel skeletons showed a similar range of variability across detection methods (Table 1). Root mean square error (RMSE) ranged from 205 m with the combined openness measurements to 954 m with negative openness. The median discrepancy indicated that all methods were more likely to under-predict the upstream extent of channel heads, but only by a few tens of meters or less in the case of positive openness, the openness combination, and channel-only geomorphons. By contrast, mean values were much lower, indicating at least some extreme channel head omissions/under-predictions, particularly among the openness maps. Standard deviations corresponded closely to RMSE values. Omission frequencies suggested that curvature exhibited somewhat lower levels of error than openness maps, whereas commission errors were low (<12%) across all methods. See Appendix B for detailed channel head detection statistics by province, land use, and site.

Table 1. Comparison of distances (in meters) between 148 observed channel head locations and 6 detection skeletons* from 14 sites across the Chesapeake Bay Basin. Omissions and commissions refer to map under and over-estmates, respectively.

Skeleton Distance	Curvature	NegOpen	PosOpen	CmbOpen	GeoChan	GeoVal
RMSE	408	954	606	205	246	287
Median	-30.5	-21.5	-6.9	-12.5	-7.9	-27.1
Mean	-113	-328	-200	-55	-44	-73
SD	394	900	574	199	243	279
Freq Omit	0.17	0.26	0.27	0.23	0.27	0.21
Freq Commit	0.04	0.07	0.03	0.04	0.11	0.11

*Curvature, openness, and GeoChan skeltons reduced using flow accumulation map and size threshold; GeoVal map reduced with a valley extent and size threshold.

Examination of the full distance distributions suggested all methods performed comparably, with substantial fractions (i.e., the IQR) of observations falling between 0 and -150 m (Figure 10). A test of the distributions revealed significant differences (Levene Test; $p<0.0017$) among group variances, thus a non-parametric test was used to compare the distributions. We found no significant difference (Kruskal-Wallis chi-square 8.51; $p=0.13$, $n=148$) associated with overall detection method despite lower negative and positive openness means.

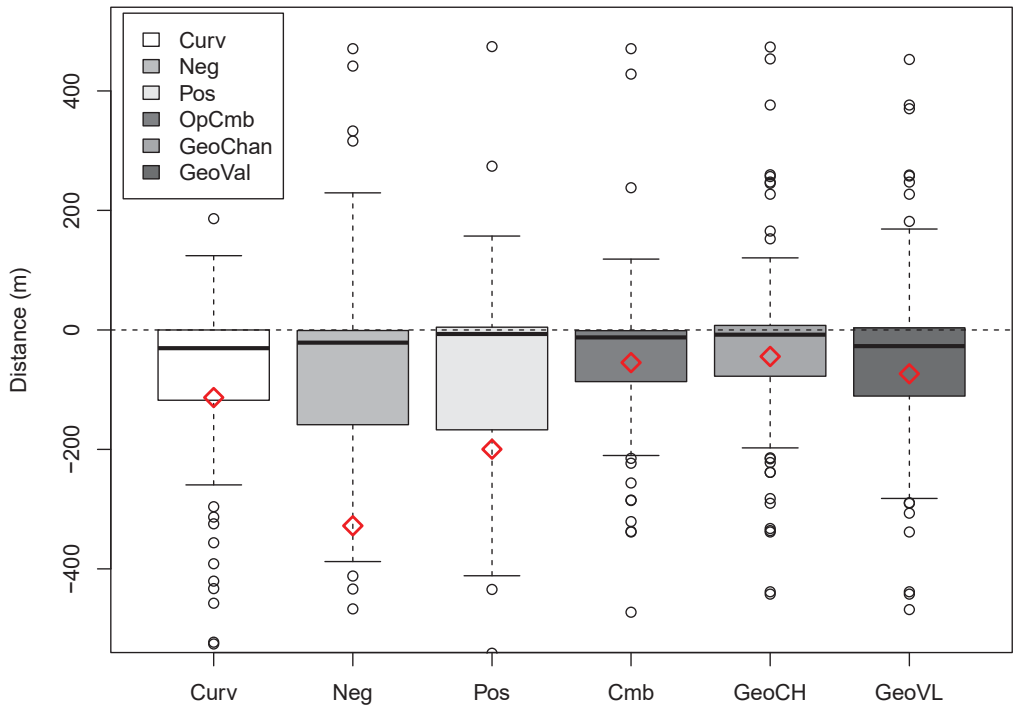

Figure 10: Boxplot comparing distances between 148 channel head locations observed in the field and locations estimated by various depression detection methods: curvature (Curv), negative openness (Neg), positive openness (Pos), combined openness (OpCmb/Cmb), geomorphon reduced by flow accumulation and areal threshold (GeoChan/GeoCH), and geomorphon reduced by valley extent and areal threshold (GeoVal/GeoVL). For each distribution, the horizontal black line represents the median, the box represents the inter-quartile range, the whiskers delimit the 10th and 90th quantiles, and circles denote outliers. Red diamonds indicate mean values.

Comparison across physiographic contexts revealed broad differences in performance (i.e., all methods were better in some provinces than others) that in some cases were also reflected within methods (e.g., one method may omit more in one physiography yet commit in another). Here, it is worth noting that unequal sample size was an important consideration in all comparisons, thus we have greater confidence in the results of certain subsets versus others. Specifically, there were only 11 channel head observations in the Valley and Ridge, 12 observations in both the outer Coastal Plain and the Valley and Ridge dominated by karst and only 15 in the Blue Ridge. Overall, provinces resulted in significant differences in the distributions of distances to observed channel heads (Kruskal-Wallis chi-square 187; df=7, $p<0.0001$, n=148). In general, channels were detected by all methods with greater efficiency in the Inner Coastal Plain and Piedmont physiographic provinces. In the Valley and Ridge province and within the glaciated Appalachian Plateau, most methods showed greater underestimates of channel extent, whereas much larger discrepancies were apparent in the Blue Ridge, the outer Coastal Plain, and the portions of the Valley and Ridge dominated by karst (Figure 11).

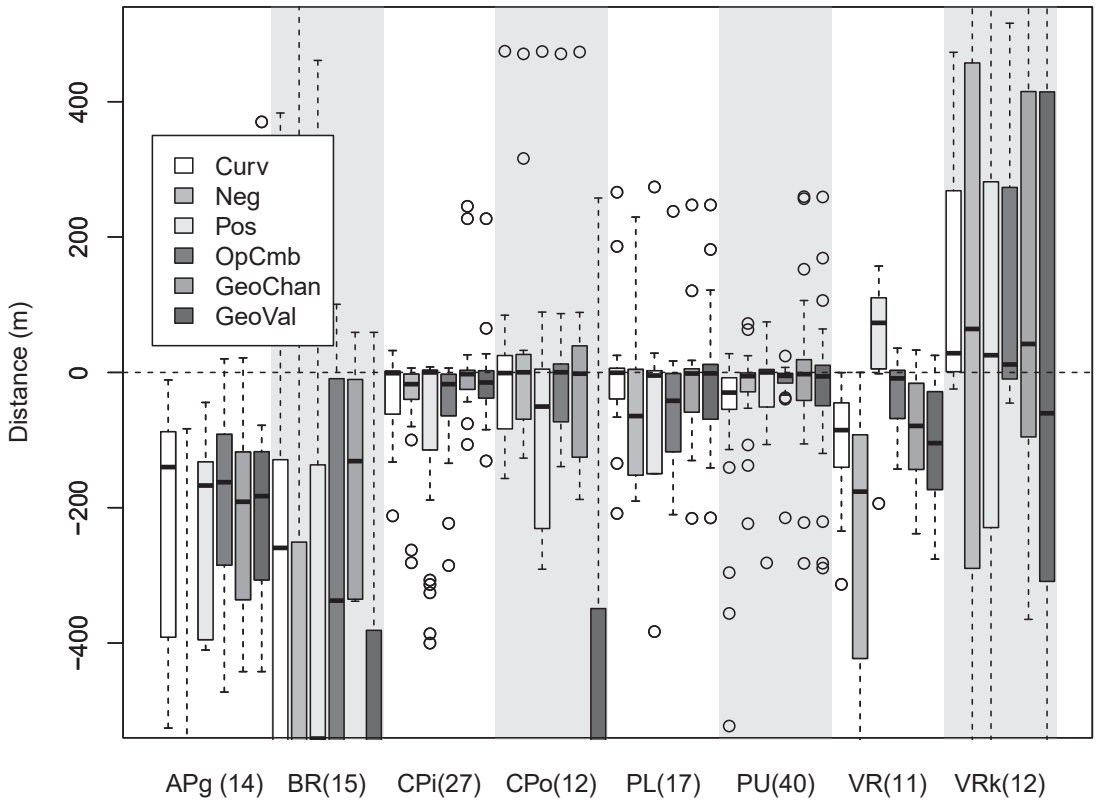

Figure 11: Boxplot comparing distances between 148 channel head locations observed in the field and locations estimated by various depression detection methods in eight physiographic contexts: glaciated Appalachian Plateau (APg), Blue Ridge (BR), inner Coastal Plain (CPi), outer Coastal Plain (CPo), Piedmont Lowlands (PL), Piedmont Uplands (PU), Valley and Ridge (VR), and karst-dominated Valley and Ridge (VRk). For each distribution, the horizontal black line represents the median, the box represents the inter-quartile range, the whiskers delimit the 10th and 90th quantiles, and circles denote outliers.

Across provinces, the interaction with detection type showed significant heterogeneity among group variances (Levene Test; $p<0.05$). These differences were also related to significant differences (Kruskal-Wallis chi-squared=22.4; df=5; $p<0.001$) in mean distance in the Appalachian Plateau, where negative openness consistently underestimated the extent of channel heads relative to other methods (Figure 11). In the Blue Ridge and Valley and Ridge with karst, small samples were not sufficient to substantiate rather large differences and variability in apparent performance. In the Blue Ridge, most field sites were located on broad, talus-dominated slopes. Here, underestimates by openness appeared to contrast with those of curvature and channel-only geomorphons, which better detected small headward channels. However, valley-network constraints imposed on geomorphons resulted in further error when channels did not occur within a clear valley feature. By contrast, in the karst terrain of the Valley and Ridge province, all methods substantially overestimated channel initiation points located in the field because direct-detection found dry channels when seepage heads occurred further downslope.

Among the remaining provinces, no difference was detected among methods for the inner Coastal Plain and the Piedmont Lowlands (Figure 11). By contrast, significant differences were detected among methods for the Outer Coastal Plain (Kruskal-Wallis chi-squared=18.5; df=5; $p=0.002$) and Piedmont Uplands (Kruskal-Wallis chi-squared=14.8; df=5; $p=0.011$). Once again, constraints imposed by broader valley delineations contributed to underestimates in the Coastal Plain. In the Piedmont Uplands, curvature showed greater underestimates than the other methods.

One area where the performance of the methods evaluated in this report clearly suffered was in geographies with extremely low relative topographic relief (e.g., talus slopes or coastal plains). Dealing with low topographic relief (i.e., signal to noise) has long been a challenge of hydrologic modelling with digital terrain data (Baker et al. 2007; Jasiewicz and Metz 2011, Passalacqua et al. 2012). This was evident in the Blackbird and Catoctin study sites (Figures 5 & 11), situated on the Delmarva Peninsula and the Blue Ridge Mountains, respectively. In both sites, channels characterized by local detection methods were excluded when delineation of the broader valley features did not extend far enough headward. This context differed from channels within well-defined valleys that are common in areas with more relief. However, geomorphons have an advantage in that one of the inputs to *r.geomorphon* is a user-specified flatness threshold. This threshold, defined as the difference (in degrees) between zenith and nadir lines of sight (below which features will be classified as flat), can be lowered in low-signal landscapes to produce a map with fewer features classified as flat. The default value of one degree was used in all study sites for this project, but we will experiment with this regional dependent threshold in future research.

Conversely, commission errors in the Valley and Ridge dominated by karst underscore one shortcoming associated with direct-detection techniques—they do not distinguish between channel-like terrain features and flowing-water channels. In this case, even visual inspection of the shaded relief suggested channels that were not corroborated in the field by even sporadic evidence of flowing water. Here, karstal flows may have diverted water from headwater channels only to emerge further downslope. Overall, the physiographic comparison in Figure 11 suggested that though all methods are capable of detecting some or most channels, curvature, combined openness, and geomorphons produced quantitatively similar results in the vast majority of contexts.

Comparison across land use contexts revealed relatively similar performance across nearly all methods but significant differences in among-group homogeneity (Levene Test $F=13.6$; $df=2$; $p<0.001$). Distances were significantly different across classes (Kruskal-Wallis chi-squared=36.8; $df=2$; $p<0.001$) and across their interaction with detection method (Kruskal-Wallis chi-squared=55.7; $df=17$; $p<0.001$), as distributions appeared far more uniform within Urban than within either Forest or Agricultural sites (Figure 12). Comparisons across methods showed no significant differences despite notable variation in among-method homogeneity (Levene Tests; $p<0.05$). Part of these differences may have resulted from the underlying physiographic variation inherent in Forested sites spanning a range of physiographic contexts, whereas Agricultural and Urban sites occurred in a more limited set of provinces.

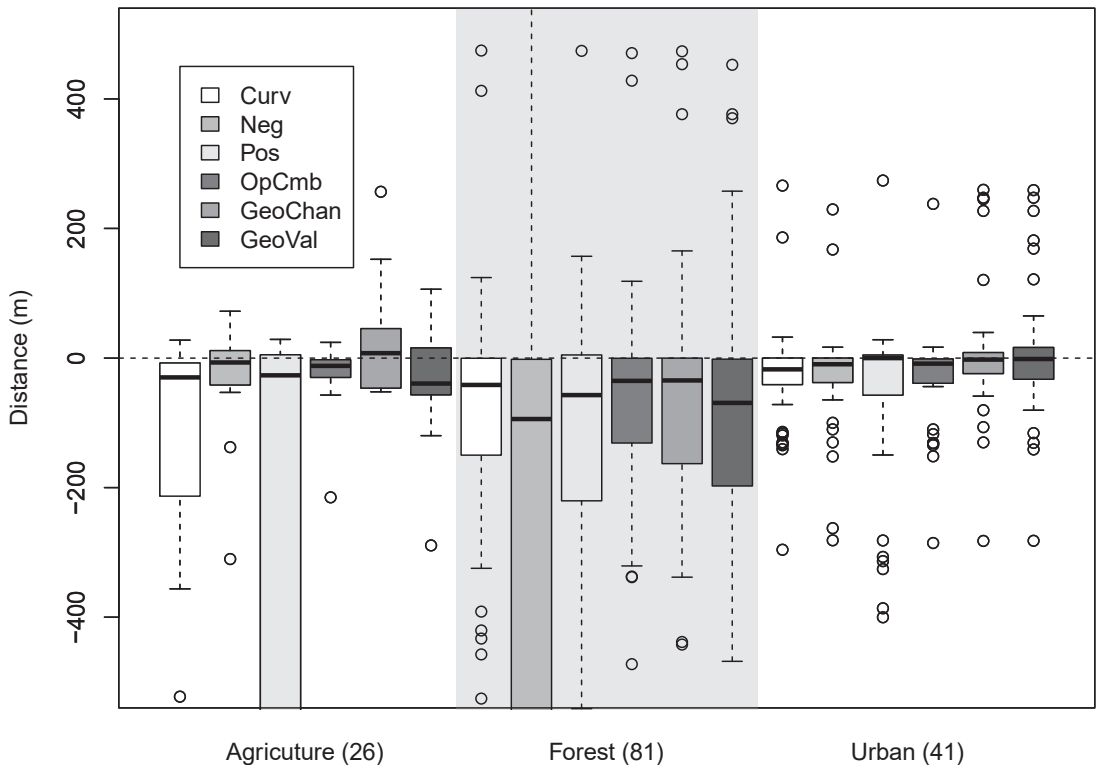

Figure 12: Boxplot comparing distances between 148 channel head locations observed in the field and locations estimated by various depression detection methods in three different land use classes. For each distribution, the horizontal black line represents the median, the box represents the inter-quartile range, the whiskers delimit the 10th and 90th quantiles, and circles denote outliers.

Overall, comparisons suggested that curvature, combined openness, and geomorphons often produced comparable detection results. However, generation of channel skeletons revealed an important shortcoming of regional topographic thresholds. Reliance on thresholds determined from the statistical distribution of values (i.e. departures from a normal QQ plot) made the results very susceptible to human alterations of the landscape or anomalies in the DEM used for analysis. Such alterations could radically change the distribution of terrain values resulting in features such as stream channels not meeting threshold criteria, even when they have a distinct topographic signature. For example, the Gettysburg study site contained a nearby quarry with extremely steep walls that skewed distribution of topographic values so that very few stream channels in the surrounding area met the QQ-derived threshold (Figure 13). At the Herbert Run site, a modified DEM rather than the terrain itself caused a similar phenomenon (Figure 14). The DEM was obtained with deep, single-pixel-width hydro-enforcement channels already burned in, and these "burned" channels skewed the distribution of terrain values in the same way as steep quarry walls in the Gettysburg DEM. We observed a similar phenomenon at the Gunpowder Falls site to a somewhat lesser degree, which used the same DEM as Herbert Run. Channel maps created using geomorphons at all three sites appeared unaffected by such anomalies because their delineation relies on spatial, as opposed to statistical, distributions of topography.

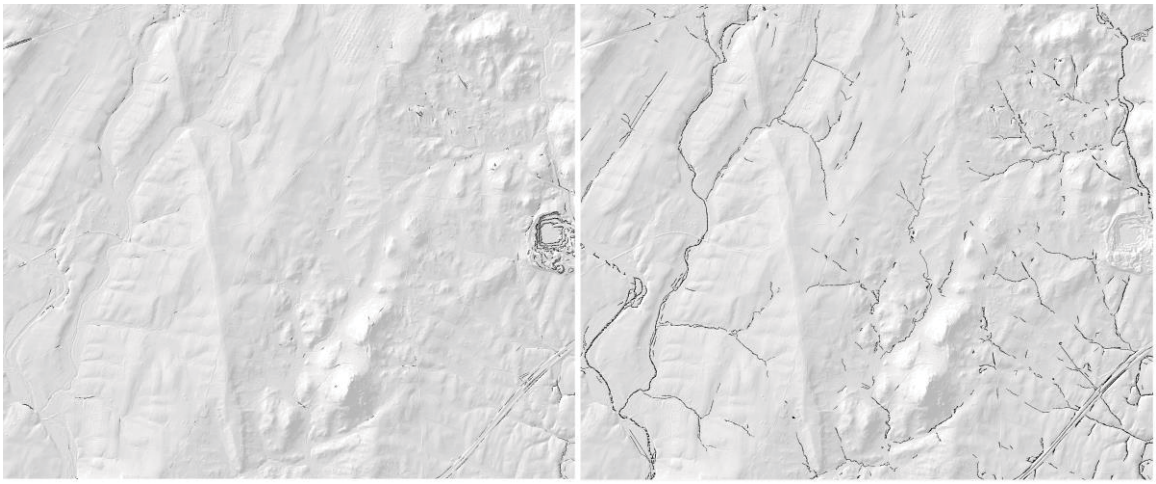

Figure 13: Channel skeletons delineated using QQ-derived threshold of curvature (left) and geomorphons (right). The quarry on the eastern edge of this study area skews the distribution of curvature values such that the QQ-threshold excludes almost all curvature pixels in the entire study area except those in the quarry. The geomorphon stream map is unaffected by the quarry and maps channel features throughout the study area.

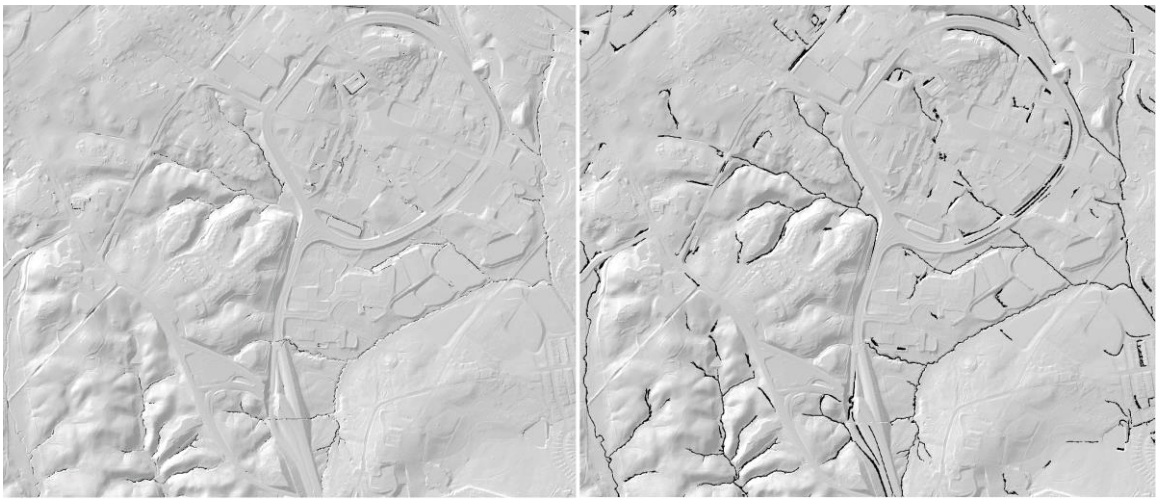

Figure 14: Channel skeletons delineated using QQ-derived threshold of curvature (left) and geomorphons (right). A hydro-enforcement channel carved perpendicular to the highway in the bottom middle of the DEM skewed the distribution of curvature values such that the threshold excludes or severely fragments stream channels with distinguishable topographic signature (e.g., bottom left, right edge). This local anomaly does not affect channel skeletons delineated using geomorphons.

The project team found that roadside and agricultural ditches were often identified by the geomorphon approach in much in the same way as stream channels. Depending on the context, these ditches may or may not be desirable in a resultant stream map. For example, if a ditch was not connected to a stream but instead functioned as detention basin along a road, it may not be desirable to include in a stream network map. However, if a ditch was directly connected to a stream via an outfall, then it could be interpreted as another channel in the network. Regardless, the fact that the geomorphon approach was capable of identifying ditches should prove valuable and will certainly be explored in-depth in future research related to ditch mapping.

Effects of geomorphic and cartographic elimination on channel skeletons

In addition to detecting depressions, we compared the impacts of various elimination methods used to remove spurious pixels from depression maps. Specifically, it was of interest to quantify the

number detections removed by geomorphic (i.e. threshold flow accumulation or valley contiguity) versus cartographic (i.e. histogram-derived area threshold) approaches (Figure 15). Moreover, this comparison was informative regarding the processing requirements for each detection method. For example, the flow accumulation elimination approach advocated by Passalacqua et al. (2012) and Sangireddy et al. (2016) requires a fully developed flow field in order to successfully reduce spurious detections in skeletons. Flow field development from LiDAR involves overcoming roadways, bridges, culverts, and other apparent obstructions to flow. Although there are algorithms to accomplish this task, none are fully automated due to the unique circumstances of stream crossings in the broader landscape, and all are computationally intensive. By contrast, elimination by connection to river valleys employed in the case of geomorphons required far less processing as a simple overlay analysis. Using the smoothed, 10-m NED DEM, it took just 10 hours to classify river valleys for the entire Chesapeake Bay watershed.

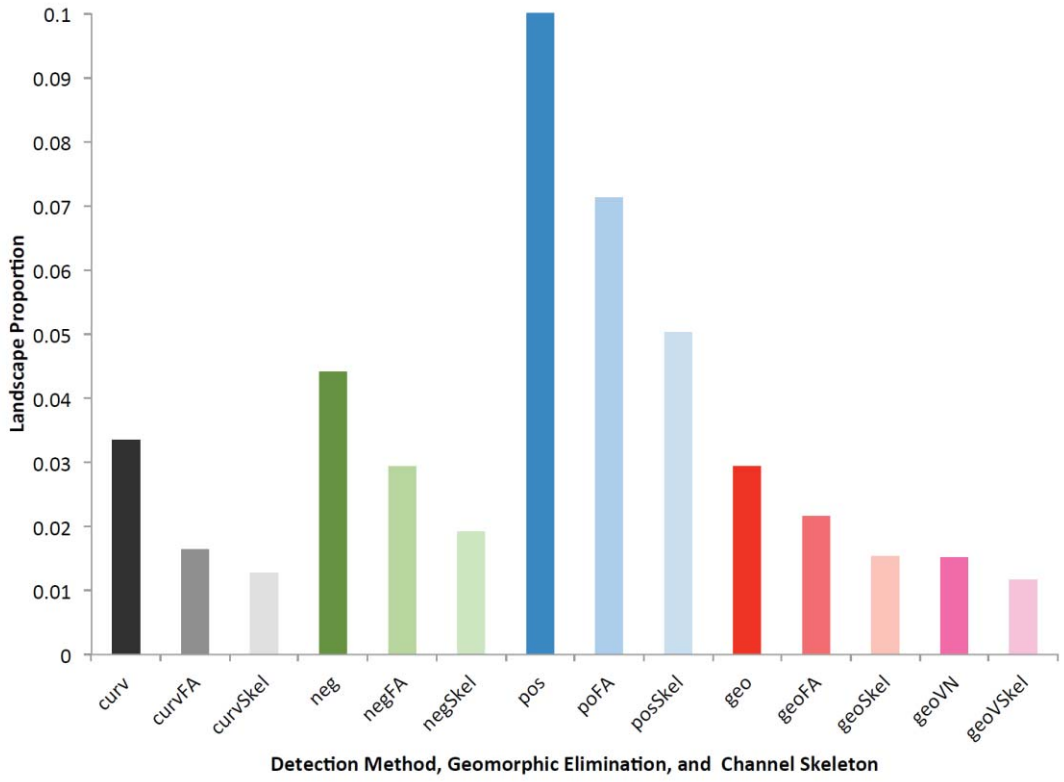

Figure 15: Comparison of raster cells identified as depressions by each of four detection methods: (1) Curvature (gray), (2) Negative Openness (green), (3) Positive Openness (blue), (4) Geomorphons filtered by flow accumulation (red), and Geomorphons filtered by connection to valley network (pink) as an average proportion of the surrounding landscape. Subsequent columns quantify the pixels remaining following a geomorphic removal (i.e., by flow accumulation threshold or valley extent) and cartographic removal to obtain the channel skeletons.

Analysis of pixel counts indicates that during initial detection, positive openness identified far more pixels than any other technique and geomorphons the least, on average. Site-specific interpretation (Appendix C) confirms this observation. Positive openness identified far greater fractions of the landscape as depressions at every site. Although geomorphons did not always identify the smallest landscape proportions, it showed the smallest variation across sites (i.e., SD~1%). Both curvature and negative openness showed intermediate detection proportions, yet twice the variability across sites. Site-specific analysis revealed that when curvature and openness detected fewer depressions pixels than geomorphons, such detections were driven by topographic anomalies (e.g., open pit mines and hydrologically enforced terrain discussed earlier) that artificially inflated thresholds

and lead to lower detection rates. Under anomalous topographic thresholds, curvature and openness were less effective at detecting channels than geomorphons.

Geomorphic removal (by flow accumulation or valley network) was substantial among all methods, but especially so for curvature and geomorphons, where the average rates exceeded 44% or nearly half the initial pixels (Figure 15). For negative and positive openness measures the removals were less extensive, averaging 36% and 29%, respectively. By contrast, the inverse pattern prevailed for cartographic removal, where curvature and geomorphon experienced only 11-12% removal, whereas the openness measures experienced 20-22%. The resulting skeletons retained between 51% (positive openness) and 57% (all others) of the initial pixels on average. These patterns suggest that when curvature and geomorphons produced spurious results, they were more likely to be in locations with small contributing areas. By contrast, positive and negative openness results produced greater spurious results overall, resulting in fewer removals by either geomorphic or cartographic approaches. Combination of positive and negative skeletons apparently further mitigated the number of spurious detections, resulting in more effective performance noted above.

Rationale for selecting skeleton delineation method

Our collective experience exploring and assessing direct-detection methods and spurious elimination techniques led to the selection of geomorphons as the terrain analysis of choice for delineating channel skeletons. First and most importantly, geomorphon was the *only* technique that did not require empirical determination of a local statistical threshold value for delineating depressions. Our experience suggested that empirical analysis using QQ plots did not lend itself well to automation, being susceptible to statistical artifacts and terrain anomalies. Although the approach appeared to work reasonably well in many cases, small differences in the critical threshold values could nonetheless lead to large differences in depression delineation, calling into question the objectivity and reproducibility of this approach over different areas and as human populations continue to modify terrain. With this important distinction in mind, curvature, combined openness, and geomorphons, with few exceptions, all performed comparably and reasonably well at detecting depressions, whereas individual openness metrics were far less reliable or consistent.

As a geomorphic approach for eliminating spurious detections of depression in *any* method, the flow accumulation method suggested by Passalacqua et al. (2010, 2012) and Sangireddy et al. (2016) appeared generally quite effective. Excluding depressions that occur high up on hillslopes, but without imposing a constant support area for channel generation was an entirely rational approach, particularly in unmodified topography. The drawback for this technique was that it required processing a flow field (i.e., a flow direction surface) over the *full extent* of LiDAR terrain. This step carries with it a host of embedded and process-intensive decisions about whether or not to fill sinks within the DEM surface or whether to breach dam-like features such as roads or downed trees for *every* possible flow path. Even though it is possible to automate these and similar procedures, it is impossible to do so with any assurance that they will not introduce further error into the terrain surface. For this important reason, we sought to limit flow-field processing in our method. A similar geomorphic approach was proposed by Clubb et al. (2014) involving analysis of longitudinal profiles, but like previous approaches, it presumed flow paths represent a result of landscape evolution and were thus best suited for unmodified terrain. In the highly modified landscapes of the Chesapeake Bay watershed, such approaches would have limited applicability.

In discussing channel head detection in terrain, many authors have advocated for the importance of valleys as both precursors to channel detection as well as geomorphic consequences of channel erosion (Montgomery and Dietrich 1988; Montgomery et al. 1993; Luo and Stepinski 2008; Jasiewicz and Metz 2011; Clubb et al. 2014; Hooshyar et al. 2016). For this reason, we assessed the

potential for delineations of river valleys to eliminate spurious depressions. In our initial interpretation, headwater river valleys were valley-like features assessed across broader extents (i.e., a 200 m radius) than channels. Moreover, *river* valleys were defined those valley features that were contiguous with the existing NHD hydrography. Based on the 10-m NED, we were able to delineate valleys in the Chesapeake Bay Watershed within a single day, and used channel *contiguity* with these valleys as the basis for our geomorphic elimination. Our results suggested that with two important exceptions, valley delineation produced comparably effective elimination results with far greater processing efficiency than flow accumulation thresholds. Exceptions occurred in areas of low relative relief such as the Delmarva or talus slopes, where low signal-to-noise in terrain surfaces prevented accurate valley delineations. Since our initial analysis, we have found that lowering the flatness threshold (i.e., being less conservative about what constitutes a valley-like depression) mitigates many of these errors. The second exception occurred in developed landscapes where roadway embankments produced overestimation of valley extents. In these contexts, we found that raising the flatness threshold (i.e., being more conservative about valley extents) mitigated the errors. In such landscapes, more aggressive removal was successful because channels outside of the more conservative valley delineations were typically incised due to augmented stormwater runoff from paved surfaces and thus were detected by their clear topographic signature and contiguity with downslope valleys. With these important exceptions in mind, we plan to refine the 10-m NED DEM valley delineations with LiDAR-based delineations in future work to allow for improved alignment of resulting products. We anticipate that this effort will eliminate many, if not all, of the errors observed in our analysis thus far.

Geoprocessing models

Many geoprocessing models were developed over the course of this project. Many were intermediate, serving only to iterate tasks over multiple DEMs, whereas others were designed to automate workflows. After performing the evaluations described in previous sections of this report and taking their findings into consideration, we developed (using ArcGIS Desktop 10.6) a suite of three key geoprocessing models to automate channel network development using geomorphons. These models were: 1) *Geomorphon Channel Skeleton*, 2) *Channel Skeleton Connectivity*, and 3) *Network Derivation*. Each may be employed in loops to iterate through successive DEMs or parallelized for more rapid processing.

The first model, *Geomorphon Channel Skeleton*, automates the process of channel skeleton development from geomorphon maps. This model isolates the channel-like depressions in a geomorphon map, applies geomorphic elimination via connectivity to a broader valley network, and applies cartographic elimination via histogram-derived areal thresholding (Figure 16). As input, the model uses a geomorphon map calculated at the channel extent, and a broader valley network. The first step in the workflow is isolation of an initial channel skeleton consisting of all pits and valleys from the input geomorphon map. This is done using the *Raster Calculator* expression:

```
Con(("%Input channel-extent geomorphons%" == 9) | ("%Input channel-
extent geomorphons%" == 10),"%Input channel-extent geomorphons%")
```

Where geomorphons with a code of 9 are valleys, and those with a code of 10 are pits. Following the isolation of an initial channel skeleton, geomorphic elimination by means of contiguity with the broader valley network is imposed using a *Cost Allocation* function. In this function, the valley network is used as the source raster and the initial channel skeleton is used as the cost raster. The output of this function is an allocation raster of pixels belonging to the source raster (i.e., valley network) *and* pixels from the cost raster that are contiguous with the source raster (i.e., channel-like depressions originating outside of, but connected to, the valley network). All other pixels contain NoData. Because this allocation raster includes pixels belonging to the broader valley network, the channel-like pixels must be isolated via the

Extract by Mask function, using the allocation raster as the input and the initial channel skeleton as the mask. This step completes the geomorphic elimination phase and produces a channel skeleton raster consisting of all channel-like depressions contained by, or contiguous with, the broader valley network.

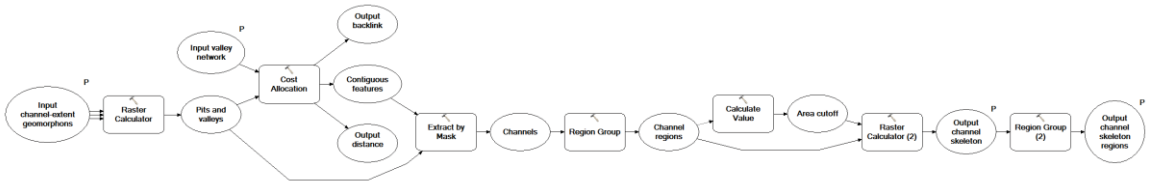

Figure 16: Geomorphon Channel Skeleton geoprocessing model. From left to right the model isolates channel-like features, discards those features not contiguous with broader valley network, and discards features not meeting a minimum area criterion.

To further reduce the skeleton raster to contain only the pixels most relevant to stream channels, cartographic elimination is applied. This is done by first performing a *Region Group* operation on the channel skeleton to identify each contiguous region of pixels and calculate the number of pixels comprising each region. This information is used as input to a *Calculate Value* script that returns a pixel count threshold for cartographic elimination. This script performs the calculations needed to produce a histogram by 1) calculating the number of unique regions in the channel skeleton, 2) calculating the number of bins in the histogram by taking the square root of the number of unique regions, and 3) calculating bin width by dividing the range of pixel counts by the number of bins. Bin width is returned and used in a *Raster Calculator* expression as the minimum pixel count required for a region of channel skeleton pixels to be retained in the final channel skeleton. This serves as cartographic elimination to remove the numerous yet small and spurious groups of pixels still remaining after geomorphic elimination. Lastly, the remaining channel skeleton is used as input to *Region Group* once more to discretize each contiguous region of the skeleton. The outputs of this model are a geomorphically- and cartographically-reduced channel skeleton consisting of pixels with a value of 1 or NoData, and a region grouped version of the same skeleton where each region has a unique ID and pixel count. An example of representative output from the *Geomorphon Channel Skeleton* geoprocessing model is presented in Figure 17.

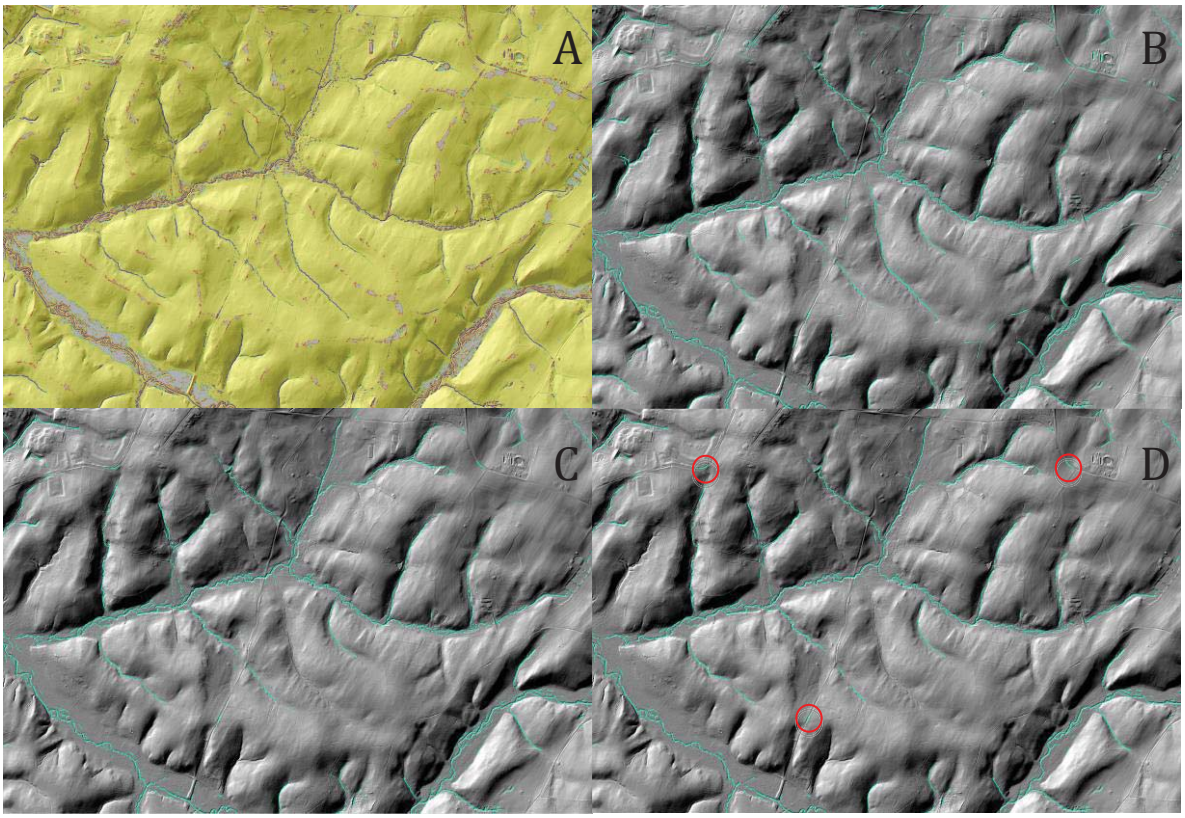

Figure 17: Representative output from the Geomorphon Channel Skeleton geoprocessing model showing the geomorphon output of valley (blue) and pit (black) features (A); isolated channel-like features overlain on shaded relief (B); channel-like features contained by the broader valley network (C); and resulting channel skeleton following areal removal (D). In C, geomorphic elimination omits several tributary channels, whereas in D, potential errors of commission along roadsides are circled in red.

In the example, the precision of the method is apparent, as are some of the typical forms of errors of both omission and commission. In this case, constraints from the valley network removed features from a few tributaries that could probably have been included, whereas several roadsides produced channel-like depressions that were retained in the output. Future work will evaluate how improved valley characterization can alleviate the former error, whereas QA/QC of output in concert with high-resolution road maps may help distinguish and mitigate the latter forms of error.

The next key geoprocessing model is called *Channel Skeleton Connectivity* and it uses the outputs from the *Geomorphon Channel Skeleton* model and a DEM to create a least-cost-connected network linking the channel skeleton regions (Figure 18). As input, this model uses the channel skeleton regions derived from the final step of the previous model, the geomorphon map calculated at the channel-extent, and DEM values restricted the extent of the valley network. First, the model uses the following *Raster Calculator* expression to create a cost surface that gives preference to convergent features at lower elevations and penalizes divergent features or those at higher elevations:

```
Con((IsNull("%Input channel regions%") & ("%Input channel-scale
geomorphon%" == 7)),(5*"%VN DEM%"),Con(IsNull("%Input channel
regions%"),(100*"%VN DEM%"),"%VN DEM%"))
```

Where geomorphons equal to 7 are classified as hollows. These features are convergent and often associated with stream channels, however they are also found frequently in other portions of the landscape and thus were not included in the channel skeleton. The cost surface weights preferential

flow along low points within the channel skeleton first, low points within hollows 5 times less, and low points outside of convergent features 100 times less. Next, the model uses the *Cost Connectivity* function to connect the channel skeleton regions along the newly created cost surface. The output of this function is a polyline connecting every region in the channel skeleton to its closest neighbors along a least-cost path (Figure 19). In practice, this operation allows a single threaded path that overcomes roadways and other dam-like obstructions occurring within valley bottoms in the LiDAR. Because the channel skeleton is already delineated, the pathways through dams or across roadways are short and more direct than would be expected from broader flow field development. The final step in this model is to rasterize the connectivity polylines for use in the next geoprocessing model.

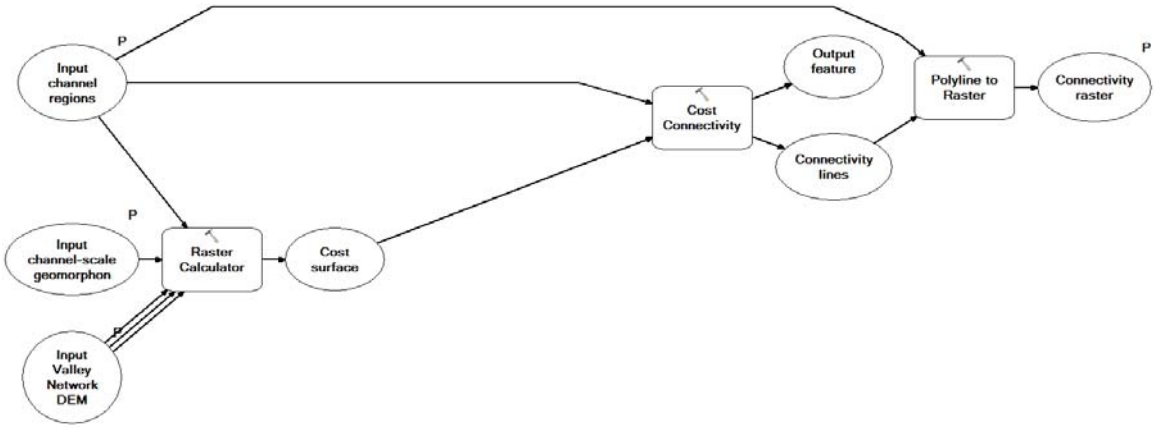

Figure 18: Channel Skeleton Connectivity geoprocessing model. From left to right the model creates a cost surface incorporating the channel skeleton, DEM, and convergent geomorphons; connects the channel skeleton along a least cost path; and converts the output to a raster.

A representative example of the output of the *Channel Skeleton Connectivity* tool is presented in Figure 19. It should be noted that while this geoprocessing model was developed in ArcGIS Desktop 10.6, trial runs frequently crashed without reporting any errors. Without making any changes to the model whatsoever, it was successfully run in ArcGIS Pro 2.2. As mentioned previously, the project team began to explore the GRASS GIS add-on *r.stream.extract* that appears to have much of the same functionality as this geoprocessing model in a more stable and computationally efficient package. We are currently investigating its applicability in our workflow.

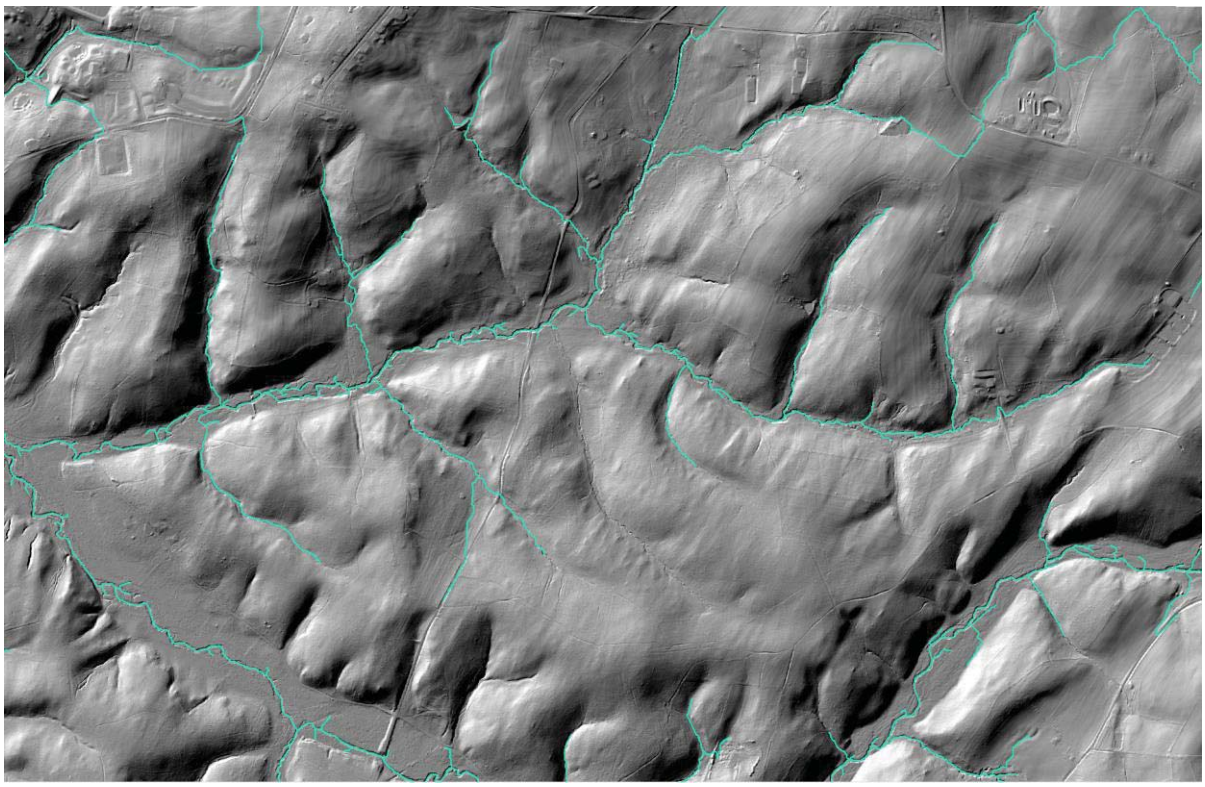

Figure 19: Representative output from the Channel Skeleton Connectivity geoprocessing model showing the results from Figure 17 linked by least-cost pathways.

The last geoprocessing model is called *Network Derivation*. This model uses the output from the previous two models to lower the elevation of the channel skeleton and least-cost paths in the DEM, compute flow directions from the altered DEM, and perform a weighted accumulation of the channel skeleton regions to produce a single-thread stream grid raster (Figure 20). As inputs, it requires DEM values restricted to the extent of the valley network, channel skeleton raster, and the connectivity raster from the previous model. First, the model "burns" the channel skeleton and least-cost connections into the valley network DEM using the following *Raster Calculator* expression:

```
Con((IsNull("%Input channel skeleton%") & IsNull("%Input connectivity
raster%")),("%VN DEM%" + 10), "%Input DEM%")
```

Following this step, depressions in the burned DEM are filled and D8 flow directions are calculated over an extent limited to the valley network. Next, a weighted flow accumulation is performed using the channel skeleton as a weight raster. This ensures that accumulation begins at the channel heads detected by geomorphons and continues downslope along the least cost paths linking the skeleton. Finally, a small threshold (e.g., 20 pixels) is applied to the weighted accumulation raster to remove very short segments from the raster and produce a single-pixel-width stream grid. It is worth noting that this step is cartographic in nature and the threshold can be chosen arbitrarily; it may need to be increased to produce a truly single-threaded grid, though it should be kept as small as possible to minimize movement of the channel head.

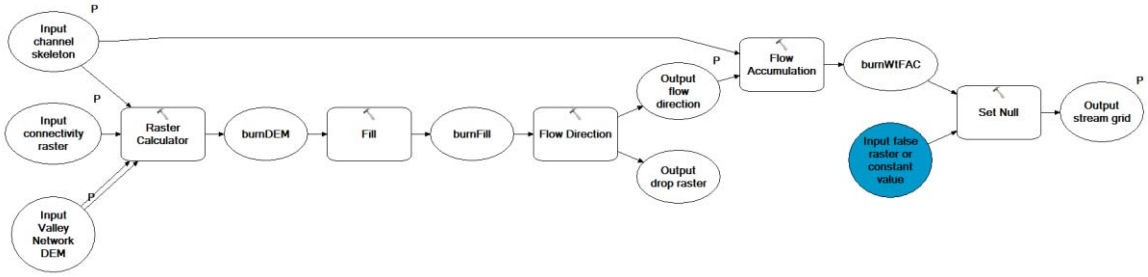

Figure 20: Network Derivation model. From left to right, the model lowers the elevation of the channel skeleton and least cost paths, fills the burned DEM, computes flow directions, computes a weighted accumulation using the channel skeleton as a weight raster, and removes very short segments not meeting a small accumulation threshold.

The purpose of this model is to create a single-pixel-width stream grid, akin to the "Str" grid produced in the ArcHydro workflow or the "src" grid produced in the TauDEM workflow. These grids are compatible with, and used as input to, various standard stream segmentation, linking, ordering, and networking tools within ArcGIS, ArcHydro, and GRASS GIS. If these outputs are not desired, it would not be necessary to run the *Network Derivation* model.

Flow permanence

Estimates of 7Q2 for January and July were obtained from the SWToolbox for all proximate gauges surrounding each study location. From gauge observations on each graph, we developed least-square fits within log-log space. We used the fitted regressions to extract drainage areas required to support flows of 0.1 cfs at each study site (Figure 21).

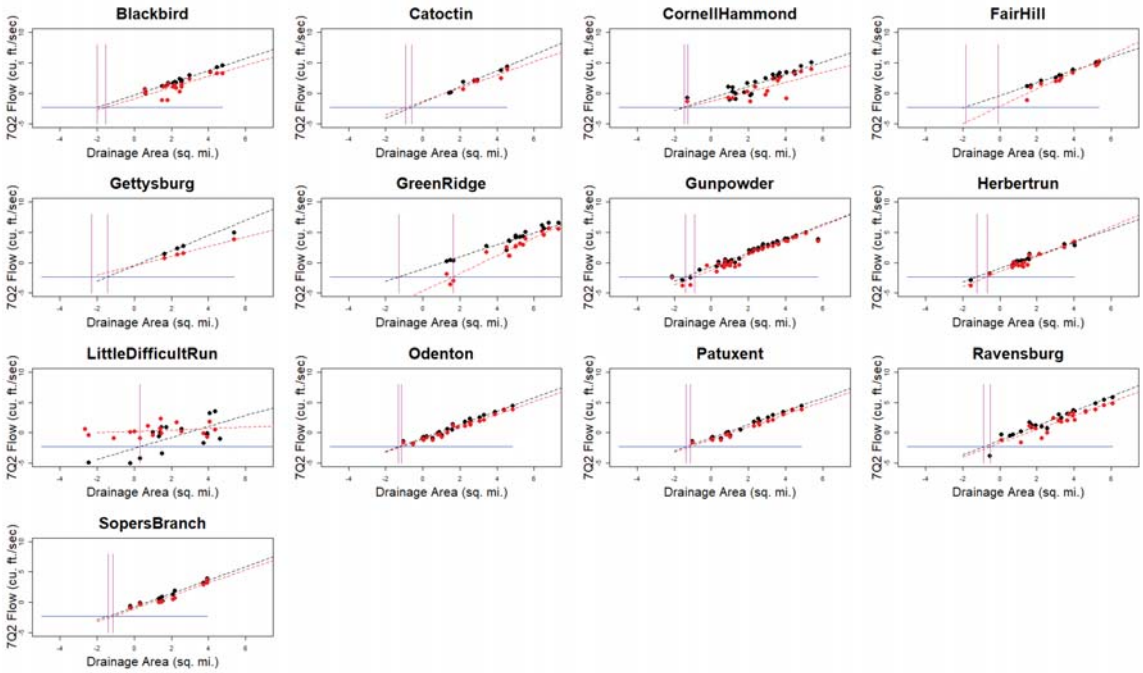

Figure 21: Plots showing relationship between drainage area and 7Q2 low flow at stream gauges surrounding each study site. 7Q2 estimates are shown as black (January) and red (July) points. Lines of best fit are shown in black (January) and red (July) dashed lines. A blue line is drawn at the threshold 7Q2 of 0.1 cfs and the intersection between lines of best fit and this threshold discharge are marked with vertical pink lines.

Summary of estimated drainage areas sufficient to generate 0.1 cfs are presented in Table 2 below. The results were fairly consistent across sites, with drainage areas between 0.2-0.3 square miles typically needed in January and larger drainage areas between 0.2-0.9 square miles required in July. Several anomalously large values were estimated for January at the Catoctin and Ravensburg sites consistent with locally important subsurface flows in karst or limestone-dominated terrain. Similarly, the area required in Little Difficult Run site was more than twice as great. This pattern suggested limited wintertime water yields in the densely urbanized landscape in which Little Difficult Run is situated. By contrast, most July estimates were 30% to 75% greater than their January counterparts as expected under greater ET demand. Exceptions to this pattern occurred in the Fair Hill site and the Green Ridge site, where areal estimates for July exceeded January by 570% and 1826%, respectively. In both cases, this pattern was driven by very low summer water yields in small drainages (Figure 21). Fair Hill was situated in an area of row crop agriculture that may be indicative of high ET demands, whereas headwaters in Green Ridge State Forest occur on a series of dry rocky ridges with limited water storage. Catoctin and Gettysburg generated anomalous July drainage area estimates that were lower than in January, a counter-intuitive result driven by lower water yields across larger drainages that lowered regression slopes. The lower yields may result from agricultural water withdrawals or losses to subsurface flow through fractured limestone and dolomite in valley floors. Little Difficult Run also showed anomalous values where baseflows remained relatively constant across all drainages; possibly due to return flow from lawn irrigation.

Table 2. Comparison of estimated drainage area required for minimum flow in January and July for 13 study sites.

	Estimated Drainage Area (sq mi) for Minimum Flow	
Site	January	July
Blackbird	0.136	0.21
Catoctin	0.551	0.401
Cornel/Hammond	0.23	0.28
Fair Hill	0.158	0.907
Gettysburg	0.238	0.102
Green Ridge	0.279	5.096
Gunpowder	0.25	0.408
Herbert Run	0.29	0.51
Little Difficult Run	1.345	0
Odenton	0.265	0.318
Patuxent	0.256	0.326
Ravensburg	0.42	0.589
Sopers Branch	0.243	0.32

Overall, our approach demonstrated potential for probabilistic delineation of ephemeral and intermittent flows based on regional regressions that provided some insight into physical or socio-cultural impacts on water yield. Importantly, our approach relied on empirical datasets and existing methods. Future work will investigate the potential for applying similar equations employed by USGS

StreamStats more broadly, or the potential for expanding the geographic area for which StreamStats can produce low-flow statistics, and evaluating the resulting estimates.

Conclusion

Accurate mapping of stream channels is a longstanding problem in the fields of geomorphology and hydrography. The methods presented in this report form a framework for automated stream channel mapping that is soundly based in geomorphic theory, computationally efficient, pragmatic, and readily applied to nearly all tested landscapes. Using concepts from computer vision to classify terrain we present a unique workflow that delineates stream channels "where they are", rather than "where they should be".

The underlying principle on which our method relies is a recent advance in the field of geomorphology called geomorphons. We used geomorphons to classify the landscape at both a broad valley extent and at a narrower channel extent. Using this information, we were able to identify depressions in the terrain corresponding to stream channels that were situated in or contiguous with broader stream valleys without expending effort trying to detect channels where they don't exist or remain disconnected from broader networks.

Our results indicate that the effectiveness of geomorphons at detecting stream channels is comparable to, or better than, other detection methods including curvature and topographic openness, employed in several stream mapping workflows published in recent years. A key advantage of geomorphons is that they are inherently multi-scalar; they are able to identify terrain features at different length scales simultaneously. Other advantages include increased computational efficiency and practicability, independence from vague or region-specific statistical thresholds, and a wealth of contextual information related to the geometry of the terrain form and its surroundings.

Although we present a robust and novel method for stream channel mapping, further research could potentially improve the results. We are only beginning to tap into the potential for geomorphons to inform our analysis by utilizing only the ten common landform classes. Many additional available outputs including the full suite of 498 unique ternary codes, shape, area, relative position, may yet inform our interpretation. This information can be used to further inform channel delineation and to characterize resulting channel maps. As we will already be mapping channel features in LiDAR with geomorphons, it makes sense in future iterations to explore valley mapping at this same level of detail, albeit with different search extents. Increased valley network precision may allow users to better assess contiguity of the network and to detect region-specific context problems such as development or low relative relief. As channel maps are derived, we expect to fully automate generation of linear flow networks compatible with the NHD.

References

Baker, M. E., Weller, D. E., & Jordan, T. E. (2006). Comparison of automated watershed delineations. *Photogrammetric Engineering & Remote Sensing*, *72*(2), 159-168.

Baker, M. E., Weller, D. E., & Jordan, T. E. (2007). Effects of stream map resolution on measures of riparian buffer distribution and nutrient retention potential. *Landscape Ecology*, *22*(7), 973-992.

Band, L. E. (1986). Topographic partition of watersheds with digital elevation models. *Water resources research*, *22*(1), 15-24.

Begin, Z. B., & Schumm, S. A. (1979). Instability of alluvial valley floors: a method for its assessment. *Transactions of the ASAE*, *22*(2), 347-0350. Beven, K.J., Kirkby, M.J. 1979. "A physically based, variable contributing area model of basin hydrology." *Hydrological Sciences Journal* 24(1): 43-69.

Bezerra, M., Baker, M., Palmer, M., Filoso, S. (In review). Sugarcane agriculture exacerbates gully formation in headwater catchments in Brazil. *Land Degradation & Development.*

Clubb, F. J., Mudd, S. M., Milodowski, D. T., Hurst, M. D., & Slater, L. J. (2014). Objective extraction of channel heads from high-resolution topographic data. *Water Resources Research*, *50*(5), 4283-4304.

Conrad, O., Bechtel, B., Bock, M., Dietrich, H., Fischer, E., Gerlitz, L., ... & Böhner, J. (2015). System for automated geoscientific analyses (SAGA) v. 2.1. 4. *Geoscientific Model Development*, *8*(7), 1991-2007.

Dietrich, W. E., & Dunne, T. (1993). The channel head. *Channel network hydrology*, 175-219.

Elmore, A. J., Julian, J. P., Guinn, S. M., & Fitzpatrick, M. C. (2013). Potential stream density in Mid-Atlantic US watersheds. *PLoS One*, *8*(8), e74819.

ESRI, R. (2011). ArcGIS desktop: release 10. *Environmental Systems Research Institute, CA*.

Gesch, D., Oimoen, M., Greenlee, S., Nelson, C., Steuck, M., & Tyler, D. (2002). The national elevation dataset. *Photogrammetric engineering and remote sensing*, *68*(1), 5-32.

GRASS Development Team. (2017). Geographic Resources Analysis Support System (GRASS) Software, Version 7.2. *Open Source Geospatial Foundation*. https://grass.osgeo.org

Hancock, G. R., & Evans, K. G. (2006). Channel head location and characteristics using digital elevation models. *Earth Surface Processes and Landforms: The Journal of the British Geomorphological Research Group*, *31*(7), 809-824.

Heine, R. A., Lant, C. L., & Sengupta, R. R. (2004). Development and comparison of approaches for automated mapping of stream channel networks. *Annals of the Association of American Geographers*, *94*(3), 477-490.

Hooshyar, M., Wang, D., Kim, S., Medeiros, S. C., & Hagen, S. C. (2016). Valley and channel networks extraction based on local topographic curvature and k-means clustering of contours. *Water Resources Research*, *52*(10), 8081-8102.

Horton, R. E. (1932). Drainage-basin characteristics. *Eos, transactions american geophysical union*, *13*(1), 350-361.

Horton, R. E. (1945). Erosional development of streams and their drainage basins; hydrophysical approach to quantitative morphology. *Geological society of America bulletin*, *56*(3), 275-370.

Howard, A. D. (1994). A detachment-limited model of drainage basin evolution. *Water resources research*, *30*(7), 2261-2285.

Ijjasz-Vasquez, E. J., & Bras, R. L. (1995). Scaling regimes of local slope versus contributing area in digital elevation models. *Geomorphology*, *12*(4), 299-311.

James, L. A., Watson, D. G., & Hansen, W. F. (2007). Using LiDAR data to map gullies and headwater streams under forest canopy: South Carolina, USA. *Catena*, *71*(1), 132-144.

Jasiewicz, J., & Metz, M. (2011). A new GRASS GIS toolkit for Hortonian analysis of drainage networks. *Computers & Geosciences*, *37*(8), 1162-1173.

Jasiewicz, J., & Stepinski, T. F. (2013). Geomorphons—a pattern recognition approach to classification and mapping of landforms. *Geomorphology*, *182*, 147-156.

Jones, D. K. (2013). *Examining development-induced geomorphic change using multi-temporal LiDAR-derived digital elevation models*. University of Maryland, Baltimore County.

Jones, D. K., Baker, M. E., Miller, A. J., Jarnagin, S. T., & Hogan, D. M. (2014). Tracking geomorphic signatures of watershed suburbanization with multitemporal LiDAR. *Geomorphology*, *219*, 42-52.

Julian, J. P., Elmore, A. J., & Guinn, S. M. (2012). Channel head locations in forested watersheds across the mid-Atlantic United States: A physiographic analysis. *Geomorphology*, *177*, 194-203. Kiang, J.E., Flynn, K.M., Zhai, T., Hummel, P., Granato, G. 2018. "SWToolbox: A surface-water tool-box for statistical analysis of streamflow time series" *U.S. Geological Survey Techniques and Methods*, book 4, chap. A–11, 33 p.

Lashermes, B., Foufoula-Georgiou, E., & Dietrich, W. E. (2007). Channel network extraction from high resolution topography using wavelets. *Geophysical Research Letters*, *34*(23).

Lindsay, J. B. (2016). Efficient hybrid breaching-filling sink removal methods for flow path enforcement in digital elevation models. *Hydrological Processes*, *30*(6), 846-857.

Luo, W., & Stepinski, T. F. (2006). Topographically derived maps of valley networks and drainage density in the Mare Tyrrhenum quadrangle on Mars. *Geophysical research letters*, *33*(18).

Luo, W., & Stepinski, T. (2008). Identification of geologic contrasts from landscape dissection pattern: An application to the Cascade Range, Oregon, USA. *Geomorphology*, *99*(1-4), 90-98.

Luo, W., & Stepinski, T. F. (2009). Computer-generated global map of valley networks on Mars. *Journal of Geophysical Research: Planets*, *114*(E11).

Maidment, D. R., & Morehouse, S. (2002). *Arc Hydro: GIS for water resources* (Vol. 1). ESRI, Inc..

Mark, D. M. (1988). Network models in geomorphology. *Modelling Geomorphological Systems. John Wiley and Sons New York. 1988. p 73-97, 11 fig, 3 tab, 60 ref. NSF Grant SES-8420789.*

McNamara, J. P., Ziegler, A. D., Wood, S. H., & Vogler, J. B. (2006). Channel head locations with respect to geomorphologic thresholds derived from a digital elevation model: A case study in northern Thailand. *Forest Ecology and Management*, *224*(1-2), 147-156.

Molloy, I., & Stepinski, T. F. (2007). Automatic mapping of valley networks on Mars. *Computers & Geosciences*, *33*(6), 728-738.

Montgomery, D. R., & Dietrich, W. E. (1988). Where do channels begin?. *Nature*, *336*(6196), 232.

Montgomery, D. R., & Dietrich, W. E. (1992). Channel initiation and the problem of landscape scale. *Science*, *255*(5046), 826-830.

Montgomery, D. R., & Foufoula-Georgiou, E. (1993). Channel network source representation using digital elevation models. *Water Resources Research*, *29*(12), 3925-3934.

Montgomery, D. R., & Dietrich, W. E. (1994). A physically based model for the topographic control on shallow landsliding. *Water resources research*, *30*(4), 1153-1171.

O'Callaghan, J. F., & Mark, D. M. (1984). The extraction of drainage networks from digital elevation data. *Computer vision, graphics, and image processing*, *28*(3), 323-344.

Passalacqua, P., Do Trung, T., Foufoula-Georgiou, E., Sapiro, G., & Dietrich, W. E. (2010). A geometric framework for channel network extraction from lidar: Nonlinear diffusion and geodesic paths. *Journal of Geophysical Research: Earth Surface*, *115*(F1).

Passalacqua, P., Belmont, P., & Foufoula-Georgiou, E. (2012). Automatic geomorphic feature extraction from lidar in flat and engineered landscapes. *Water Resources Research*, *48*(3).

Passalacqua, P., & Foufoula-Georgiou, E. (2015). Comment on "Objective extraction of channel heads from high-resolution topographic data" by Fiona J. Clubb et al. *Water Resources Research*, *51*(2), 1372-1376.

Patton, P. C., & Schumm, S. A. (1975). Gully erosion, Northwestern Colorado: a threshold phenomenon. *Geology*, *3*(2), 88-90.

Pelletier, J. D. (2013). A robust, two-parameter method for the extraction of drainage networks from high-resolution digital elevation models (DEMs): Evaluation using synthetic and real-world DEMs. *Water Resources Research*, *49*(1), 75-89.

Peucker, T. K., & Douglas, D. H. (1975). Detection of surface-specific points by local parallel processing of discrete terrain elevation data. *Computer Graphics and image processing*, *4*(4), 375-387.

Pirotti, F., & Tarolli, P. (2010). Suitability of LiDAR point density and derived landform curvature maps for channel network extraction. *Hydrological Processes: An International Journal*, *24*(9), 1187-1197.

Poesen, J., Nachtergaele, J., Verstraeten, G., & Valentin, C. (2003). Gully erosion and environmental change: importance and research needs. *Catena*, *50*(2-4), 91-133.

Rodriguez-Iturbe, I., & Rinaldo, A. (2001). *Fractal river basins: chance and self-organization*. Cambridge University Press.

Ries III, K. G., Newson, J. K., Smith, M. J., Guthrie, J. D., Steeves, P. A., Haluska, T. L., ... & Vraga, H. W. (2017). *StreamStats, version 4* (No. 2017-3046). US Geological Survey.

Sangireddy, H., Stark, C. P., Kladzyk, A., & Passalacqua, P. (2016). GeoNet: An open source software for the automatic and objective extraction of channel heads, channel network, and channel morphology from high resolution topography data. *Environmental Modelling & Software*, *83*, 58-73.

Saunders, W. (1999, July). Preparation of DEMs for use in environmental modeling analysis. In *ESRI User Conference* (pp. 24-30).

Schumm, S. A. (1979). Geomorphic thresholds: the concept and its applications. *Transactions of the Institute of British Geographers*, 485-515.

Seibert, J., & McGlynn, B. L. (2007). A new triangular multiple flow direction algorithm for computing upslope areas from gridded digital elevation models. *Water resources research*, *43*(4).

Smith, S. M. C., & Wilcock, P. R. (2015). Upland sediment supply and its relation to watershed sediment delivery in the contemporary mid-Atlantic Piedmont (USA). *Geomorphology*, *232*, 33-46.

Sofia, G., Tarolli, P., Cazorzi, F., & Dalla Fontana, G. (2011). An objective approach for feature extraction: distribution analysis and statistical descriptors for scale choice and channel network identification. *Hydrology and earth system sciences*, *15*(5), 1387-1402.

Soille, P. (2004). Optimal removal of spurious pits in grid digital elevation models. *Water Resources Research*, *40*(12).

Stock, J., & Dietrich, W. E. (2003). Valley incision by debris flows: Evidence of a topographic signature. *Water Resources Research*, *39*(4).

Sun, X., Rosin, P., Martin, R., & Langbein, F. (2007). Fast and effective feature-preserving mesh denoising. *IEEE Transactions on Visualization & Computer Graphics*, (5), 925-938.

Tarboton, D. G. (1997). A new method for the determination of flow directions and upslope areas in grid digital elevation models. *Water resources research*, *33*(2), 309-319.

Tarboton, D. G., & Ames, D. P. (2001). Advances in the mapping of flow networks from digital elevation data. In *Bridging the Gap: Meeting the World's Water and Environmental Resources Challenges* (pp. 1-10).

Tarboton, D. G., & Baker, M. E. (2008). Towards an algebra for terrain-based flow analysis. *Representing, modeling and visualizing the natural environment: innovations in GIS*, *13*, 167-194.

Tarboton, D. G., & Mohammed, I. N. (2013). TauDEM 5.1 quick start guide to using the TauDEM ArcGIS toolbox. *Utah State University (USU), United States*.

Tarolli, P., & Dalla Fontana, G. (2009). Hillslope-to-valley transition morphology: New opportunities from high resolution DTMs. *Geomorphology*, *113*(1-2), 47-56.

Tarolli, P., & Tarboton, D. G. (2006). A new method for determination of most likely landslide initiation points and the evaluation of digital terrain model scale in terrain stability mapping. *Hydrology and Earth System Sciences Discussions*, *10*(5), 663-677.

Tucker, G. E., & Bras, R. L. (1998). Hillslope processes, drainage density, and landscape morphology. *Water Resources Research*, *34*(10), 2751-2764.

U.S. Geological Survey. (2017). National Hydrography Dataset Plus High Resolution (NHDPlus HR). *USGS National Map Downloadable Data Collection.*

Weller, D. E., & Baker, M. E. (2014). Cropland riparian buffers throughout Chesapeake Bay watershed: Spatial patterns and effects on nitrate loads delivered to streams. *JAWRA Journal of the American Water Resources Association*, *50*(3), 696-712.

Wilson, J. P., & Gallant, J. C. (2000). Digital terrain analysis. *Terrain analysis: principles and applications*, *6*(12), 1-27.

Yokoyama, R., Shirasawa, M., & Pike, R. J. (2002). Visualizing topography by openness: a new application of image processing to digital elevation models. *Photogrammetric engineering and remote sensing*, *68*(3), 257-266.

Zhang, W., & Montgomery, D. R. (1994). Digital elevation model grid size, landscape representation, and hydrologic simulations. *Water resources research*, *30*(4), 1019-1028.

Appendix A

A1: Quantile-Quantile plots of curvature distributions by site (normal distribution plotted in red)

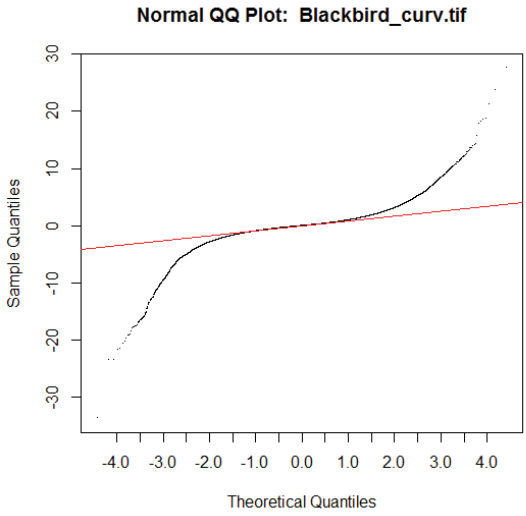

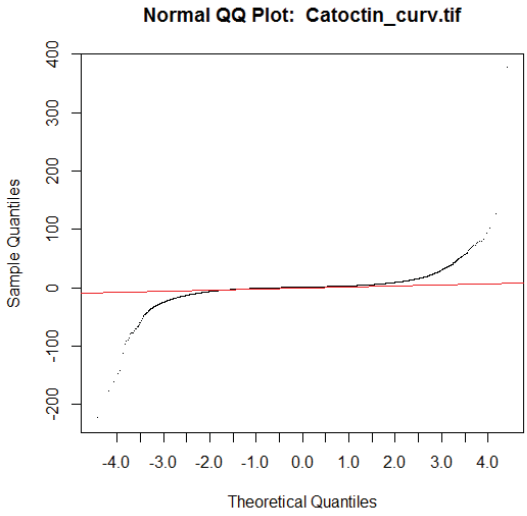

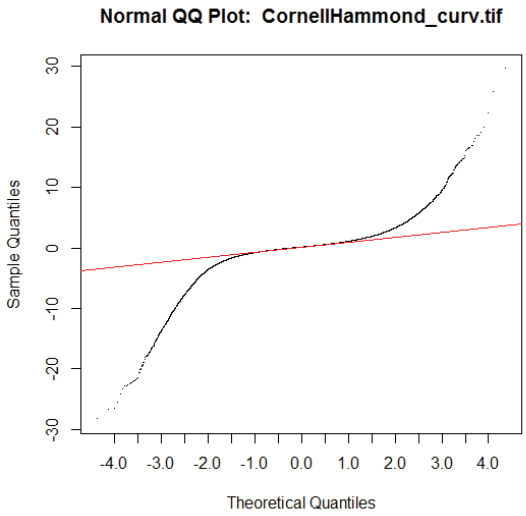

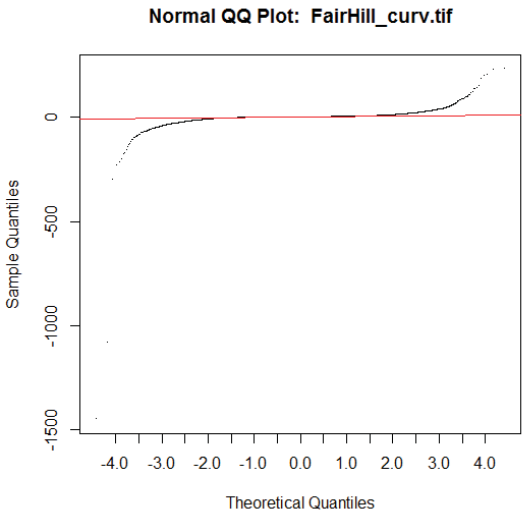

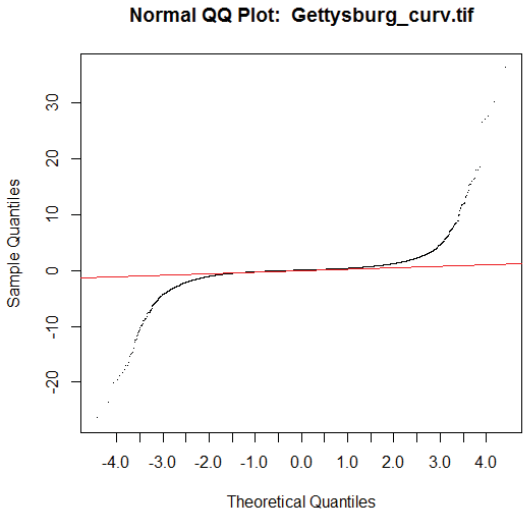
Normal QQ Plot: Gettysburg_curv.tif
Sample Quantiles
Theoretical Quantiles
-20
-10
0
10
20
30
-4.0
-3.0
-2.0
-1.0
0.0
1.0
2.0
3.0
4.0

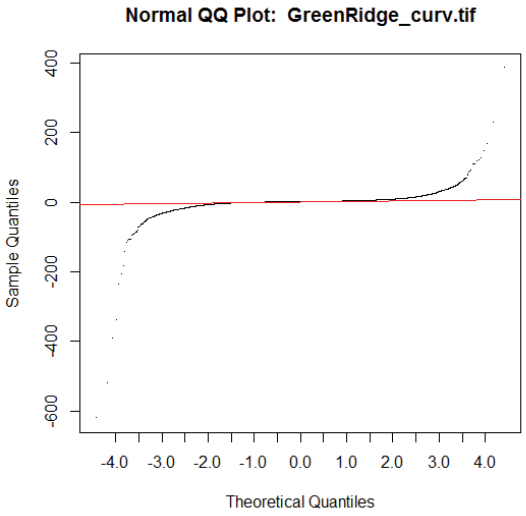
Normal QQ Plot: GreenRidge_curv.tif
Sample Quantiles
Theoretical Quantiles
-600
-400
-200
0
200
400
-4.0
-3.0
-2.0
-1.0
0.0
1.0
2.0
3.0
4.0

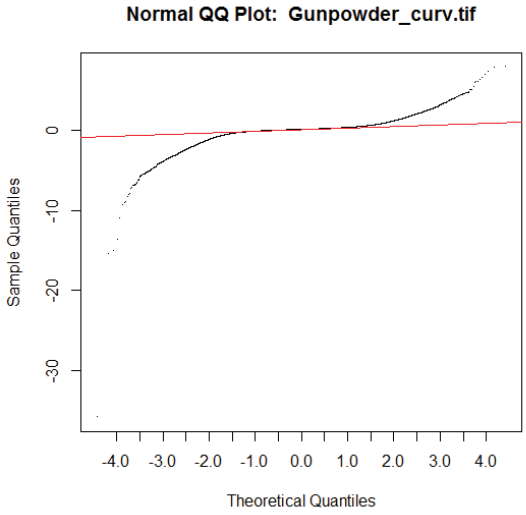
Normal QQ Plot: Gunpowder_curv.tif
Sample Quantiles
Theoretical Quantiles
-30
-20
-10
0
-4.0
-3.0
-2.0
-1.0
0.0
1.0
2.0
3.0
4.0

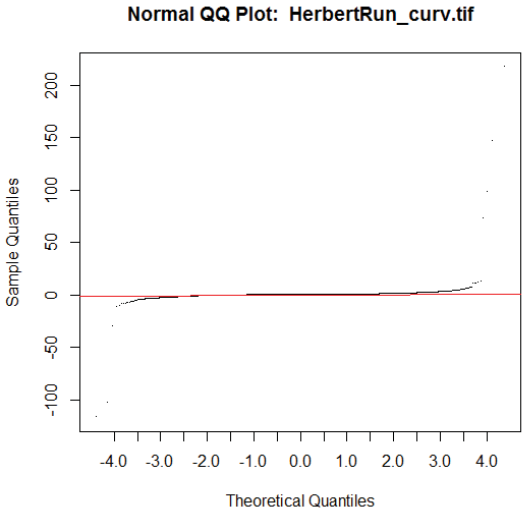
Normal QQ Plot: HerbertRun_curv.tif
Sample Quantiles
Theoretical Quantiles
-100
-50
0
50
100
150
200
-4.0
-3.0
-2.0
-1.0
0.0
1.0
2.0
3.0
4.0

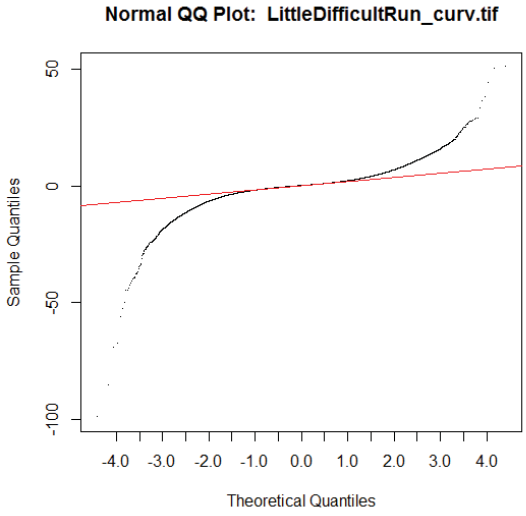
Normal QQ Plot: LittleDifficultRun_curv.tif
Sample Quantiles
Theoretical Quantiles
-100
-50
0
50
-4.0
-3.0
-2.0
-1.0
0.0
1.0
2.0
3.0
4.0

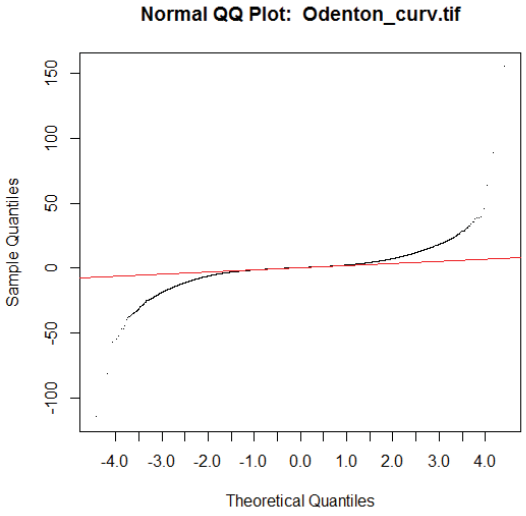
Normal QQ Plot: Odenton_curv.tif
Sample Quantiles
Theoretical Quantiles
-100
-50
0
50
100
150
-4.0
-3.0
-2.0
-1.0
0.0
1.0
2.0
3.0
4.0

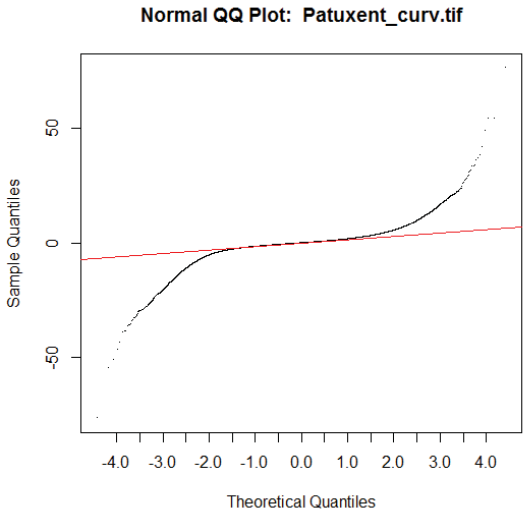
Normal QQ Plot: Patuxent_curv.tif
Sample Quantiles
Theoretical Quantiles
50
0
-50
-4.0
-3.0
-2.0
-1.0
0.0
1.0
2.0
3.0
4.0

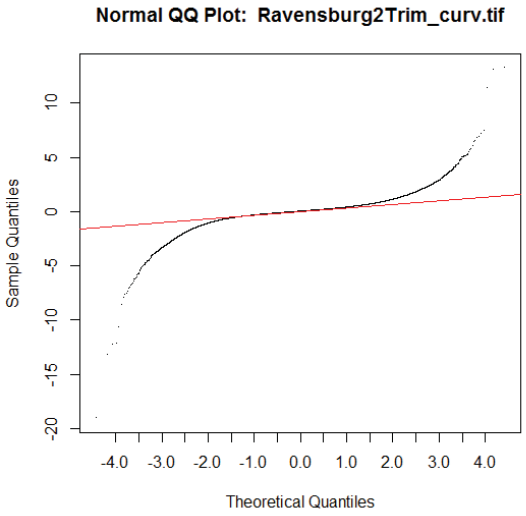
Normal QQ Plot: Ravensburg2Trim_curv.tif
Sample Quantiles
Theoretical Quantiles
10
5
0
-5
-10
-15
-20
-4.0
-3.0
-2.0
-1.0
0.0
1.0
2.0
3.0
4.0

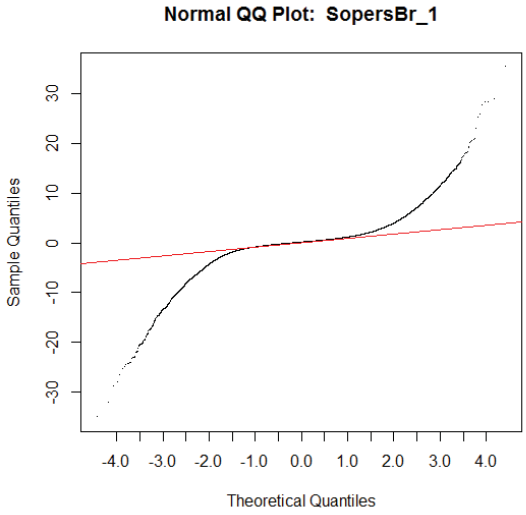
Normal QQ Plot: SopersBr_1
Sample Quantiles
Theoretical Quantiles
30
20
10
0
-10
-20
-30
-4.0
-3.0
-2.0
-1.0
0.0
1.0
2.0
3.0
4.0

A2: Quantile-Quantile plots of positive openness distributions by site (normal distribution plotted in red)

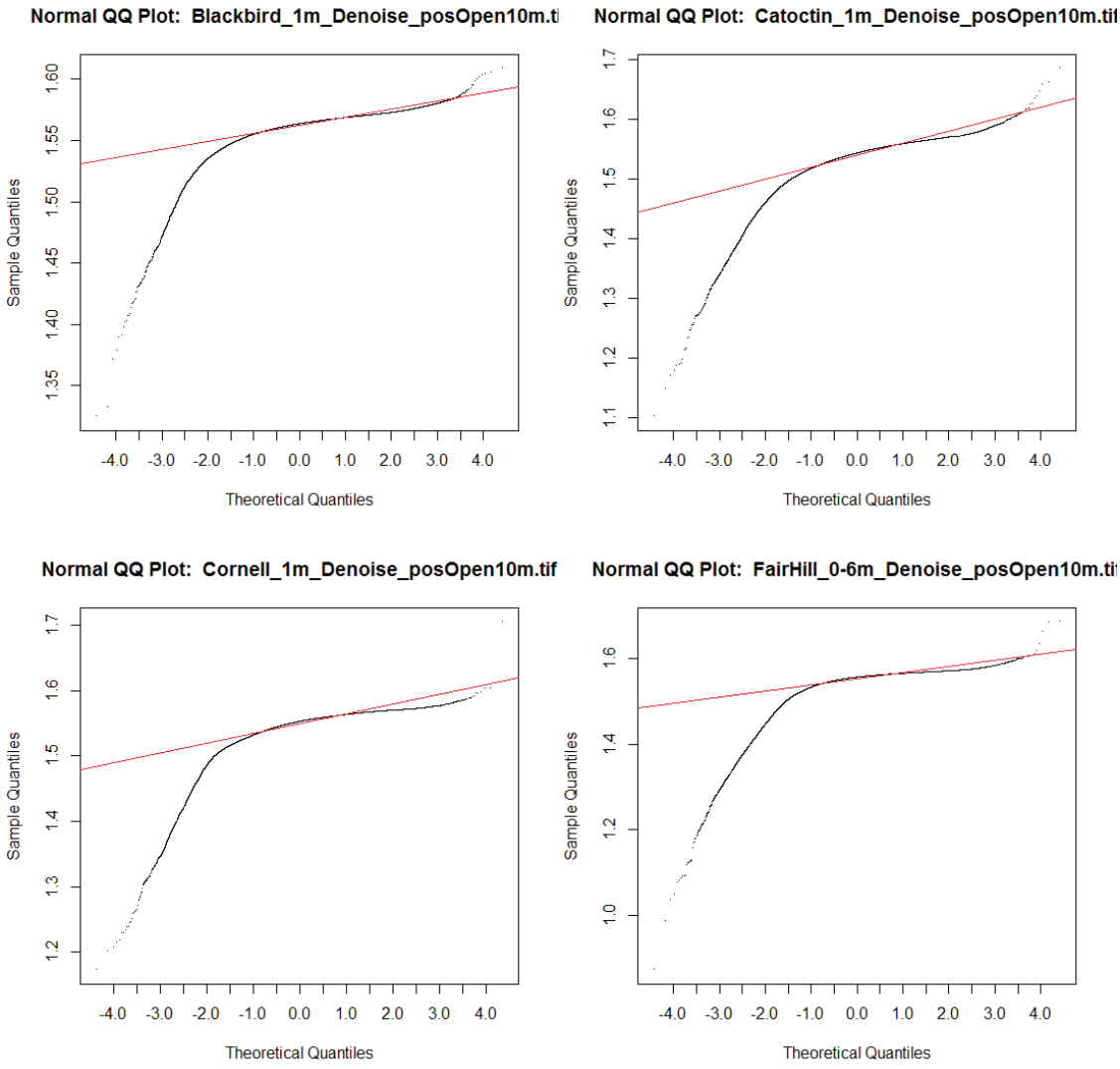

Normal QQ Plot: Gettysburg_3ft_Denoise_posOpen10m.t

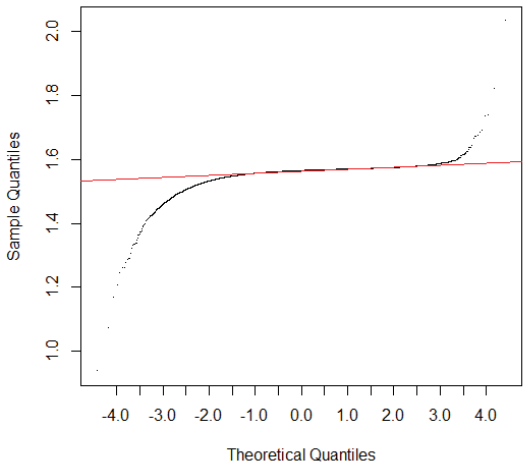

Normal QQ Plot: GreenRidge_1m_Denoise_posOpen10m.

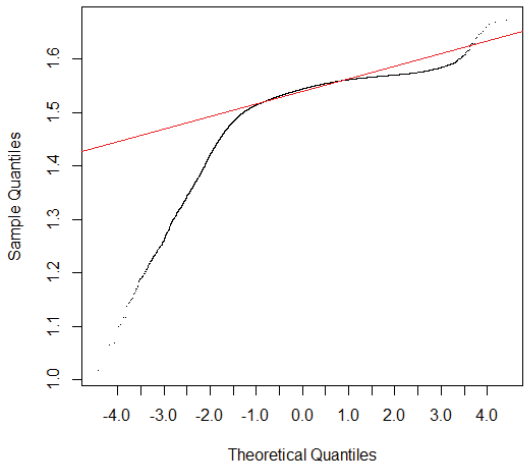

Normal QQ Plot: Gunpowder_2-5ft_Denoise_posOpen10m

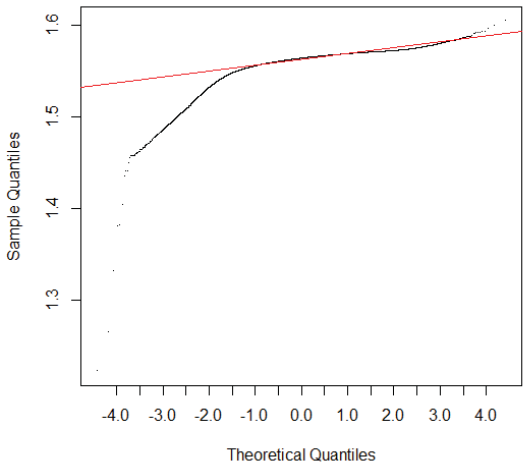

Normal QQ Plot: HerbertRun_2-5ft_Denoise_posOpen10m

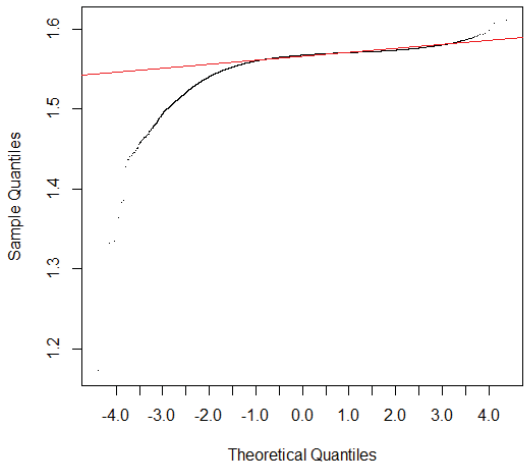

Normal QQ Plot: LittleDifficultRun_1m_Denoise_posOpen10

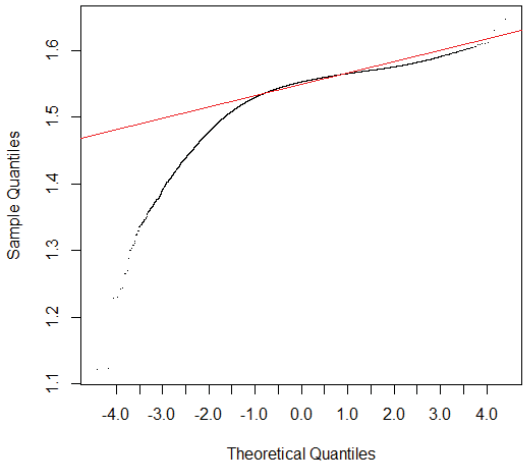

Normal QQ Plot: Odenton_0-9m_Denoise_posOpen10m.t

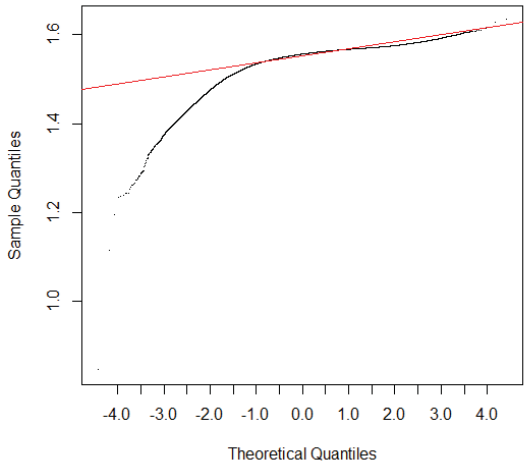

Normal QQ Plot: Patuxent_0-9m_Denoise_posOpen10m.brmal QQ Plot: Ravensburg_3-28ft_DenoiseTrim_posOpen1

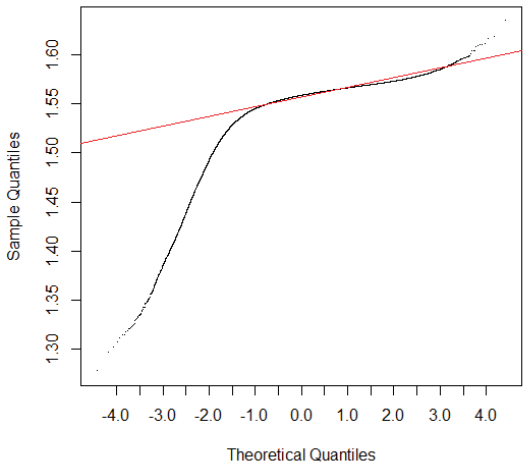

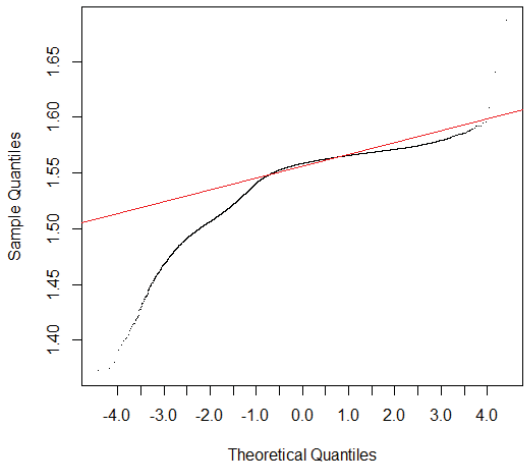

Normal QQ Plot: SopersBranch_1-2m_Denoise_posOpen10

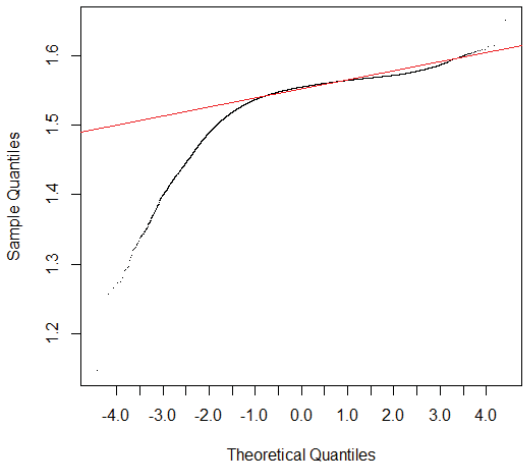

A3: Quantile-Quantile plots of negative openness distributions by site (normal distribution plotted in red)

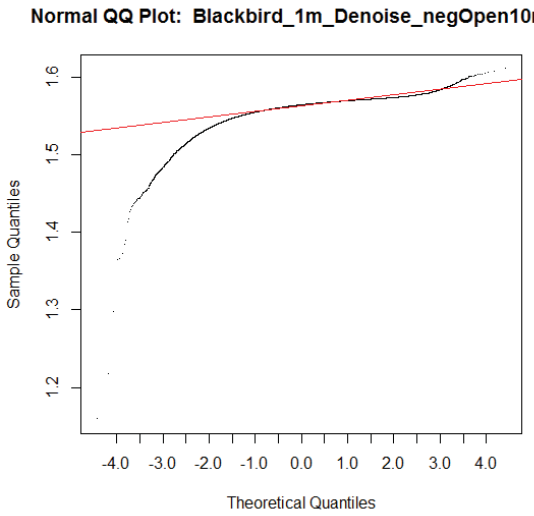

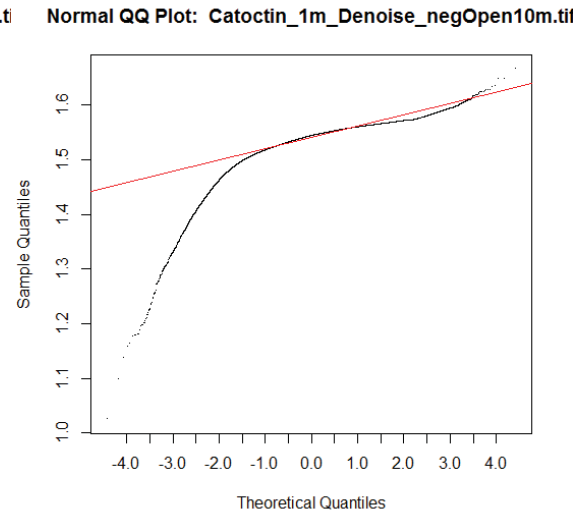

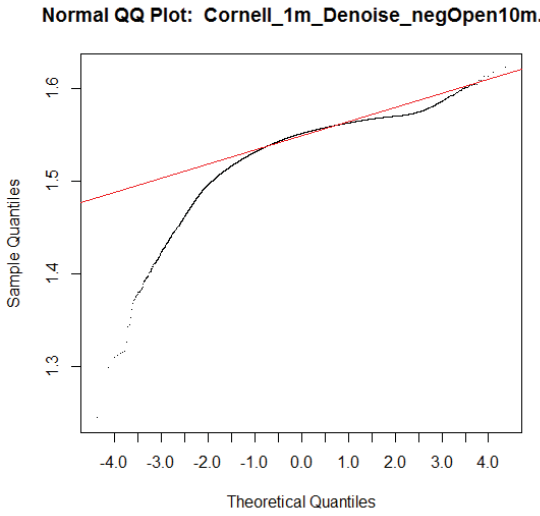

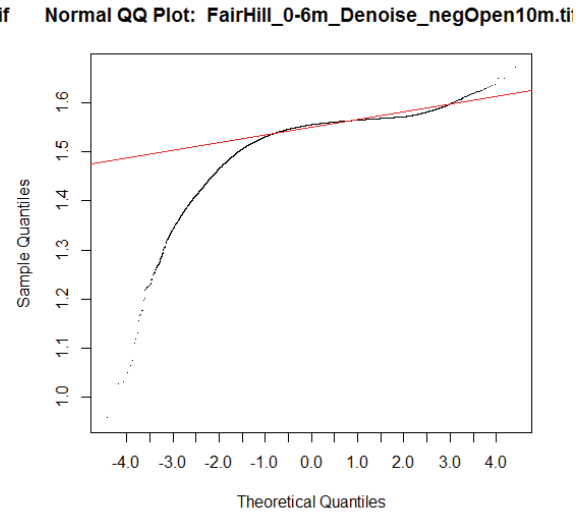

Normal QQ Plot: Gettysburg_3ft_Denoise_negOpen10m.

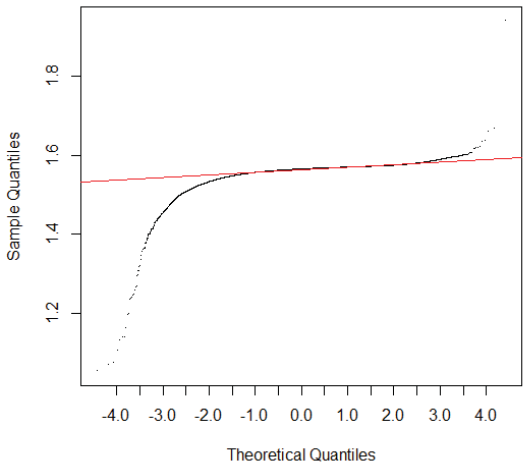

Normal QQ Plot: GreenRidge_1m_Denoise_negOpen10m.

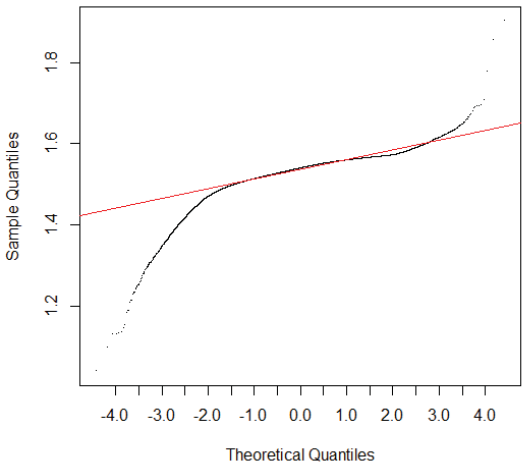

Normal QQ Plot: Gunpowder_2-5ft_Denoise_negOpen10m

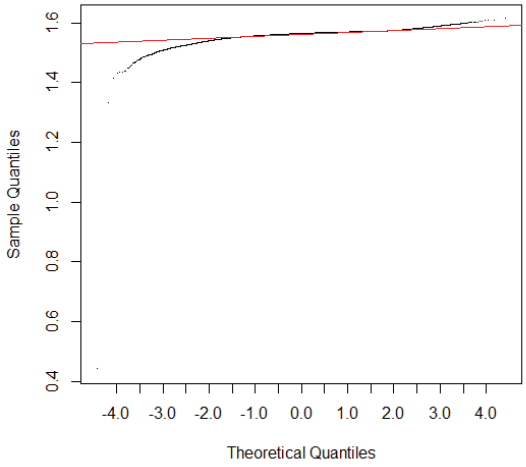

Normal QQ Plot: HerbertRun_2-5ft_Denoise_negOpen10m

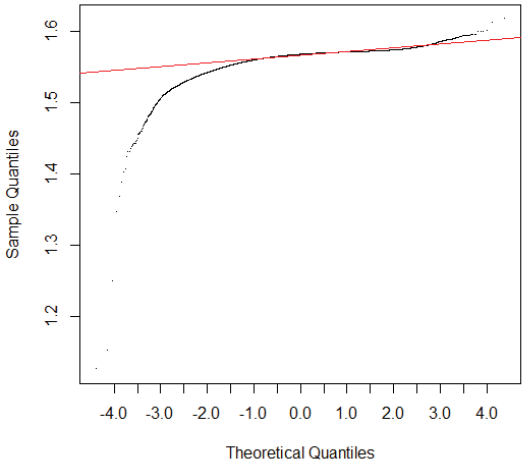

Normal QQ Plot: LittleDifficultRun_1m_Denoise_negOpen10

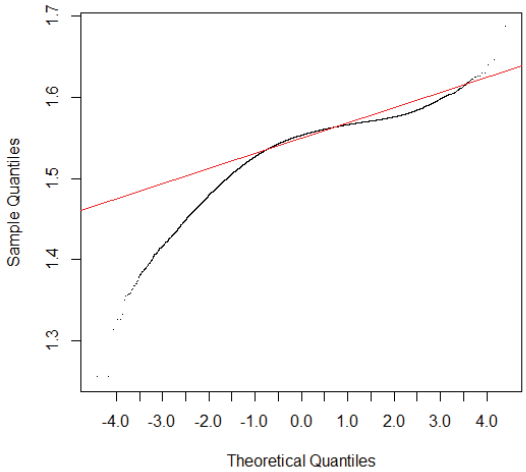

Normal QQ Plot: Odenton_0-9m_Denoise_negOpen10m.t

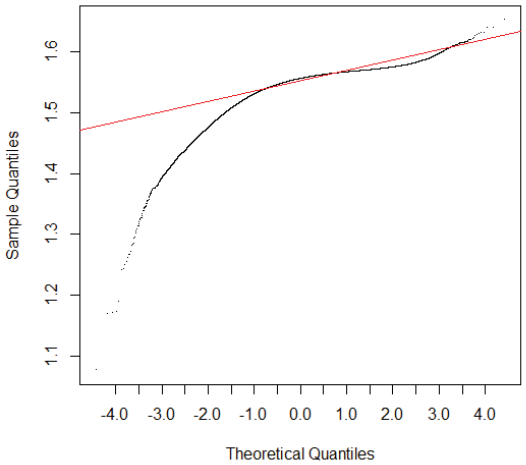

Normal QQ Plot: Patuxent_0-9m_Denoise_negOpen10m.brmal QQ Plot: Ravensburg_3-28ft_DenoiseTrim_negOpen1

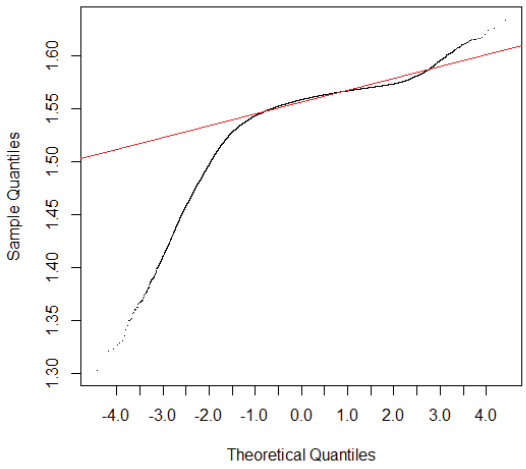

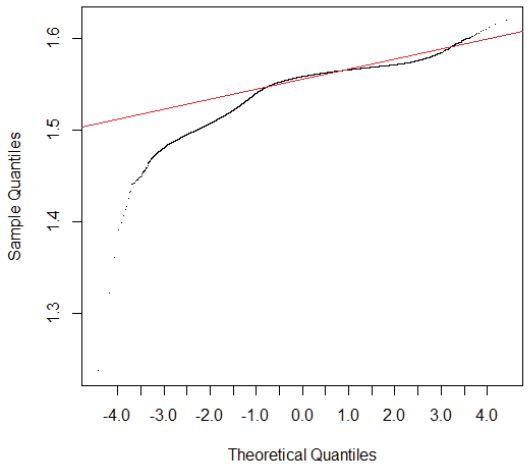

Normal QQ Plot: SopersBranch_1-2m_Denoise_negOpen10

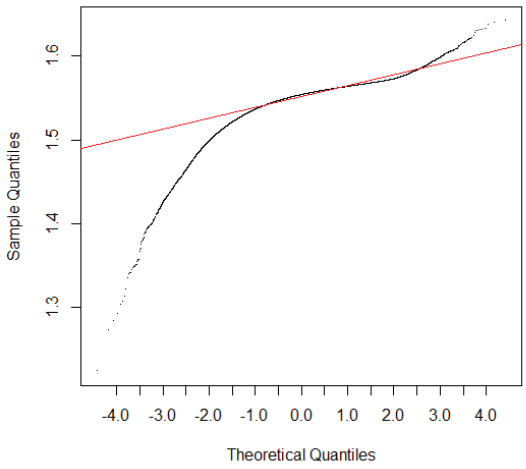

A4: Site-specific quantile-quantile thresholds of curvature, positive openness, and negative openness

Site	Landuse	Province	Method	Theoretical Quantile	Empircal value
Blackbird	Ag	Coastal Plain outer	Curvature	-1.25	-1.91
Blackbird	Ag	Coastal Plain outer	Positive Openness	-1	1.55
Blackbird	Ag	Coastal Plain outer	Negative Openness	1	1.571
Catoctin	Forest	Blue ridge	Curvature	-1.75	-8.08
Catoctin	Forest	Blue ridge	Positive Openness	-1	1.508
Catoctin	Forest	Blue ridge	Negative Openness	1	1.566
Cornell/Hammond	Ag/Forest	Appalachian Plateau glaciated	Curvature	-1	-1.79
Cornell/Hammond	Ag/Forest	Appalachian Plateau glaciated	Positive Openness	-1	1.522
Cornell/Hammond	Ag/Forest	Appalachian Plateau glaciated	Negative Openness	1	1.566
Fair Hill	Ag	Piedmont Upland	Curvature	-1.7	-15.23
Fair Hill	Ag	Piedmont Upland	Positive Openness	-1	1.513
Fair Hill	Ag	Piedmont Upland	Negative Openness	1	1.574
Gettysburg	Ag	Piedmont Upland	Curvature	-1.6	-1.92
Gettysburg	Ag	Piedmont Upland	Positive Openness	-1	1.549
Gettysburg	Ag	Piedmont Upland	Negative Openness	1	1.574
Green Ridge	Forest	Valley and Ridge no karst	Curvature	-1.8	-10.36
Green Ridge	Forest	Valley and Ridge no karst	Positive Openness	-1	1.495
Green Ridge	Forest	Valley and Ridge no karst	Negative Openness	1	1.563
Gunpowder	Forest	Piedmont Upland	Curvature	-1.3	-1.86
Gunpowder	Forest	Piedmont Upland	Positive Openness	-1	1.55
Gunpowder	Forest	Piedmont Upland	Negative Openness	1	1.57
Herbert Run	Urban	Piedmont Upland	Curvature	-2.6	-2.38
Herbert Run	Urban	Piedmont Upland	Positive Openness	-1	1.555
Herbert Run	Urban	Piedmont Upland	Negative Openness	1	1.573
Little Difficult Run	Urban	Piedmont Lowland	Curvature	-1.2	-3.93
Little Difficult Run	Urban	Piedmont Lowland	Positive Openness	-1	1.522
Little Difficult Run	Urban	Piedmont Lowland	Negative Openness	1	1.57
Odenton	Urban	Coastal Plain inner	Curvature	-1.25	-4.19
Odenton	Urban	Coastal Plain inner	Positive Openness	-1	1.523
Odenton	Urban	Coastal Plain inner	Negative Openness	1	1.574
Patuxent	Forest	Coastal Plain inner	Curvature	-1.5	-4.3
Patuxent	Forest	Coastal Plain inner	Positive Openness	-1	1.532
Patuxent	Forest	Coastal Plain inner	Negative Openness	1	1.573
Ravensburg	Forest	Valley and Ridge karst	Curvature	-1.5	-0.85
Ravensburg	Forest	Valley and Ridge karst	Positive Openness	-1	1.536
Ravensburg	Forest	Valley and Ridge karst	Negative Openness	1	1.569
Sopers Branch	Forest	Piedmont Lowland	Curvature	-1.25	-2.64
Sopers Branch	Forest	Piedmont Lowland	Positive Openness	-1	1.527
Sopers Branch	Forest	Piedmont Lowland	Negative Openness	1	1.568

Appendix B

B1: Channel head detection statistics by physiographic province

Appendix B1. Comparison of distances (in meters) between 148 observed channel head locations and 6 detection skeletons* from 14 sites in eight physiographic provinces across the Chesapeake Bay Basin. Omissions and commissions refer to map under and over-estmates, respectively.

Statistic	Province	Curvature	NegOpen	PosOpen	CmbOpen	GeoChan	GeoVal
RMSE	App Plat (g)	270.4	2651.1	1505.5	263.4	521.9	540.2
	Blue Ridge	736.9	1418.8	1463.7	5794.7	544.7	1164.3
	Cst Pln (i)	69.0	234.3	159.3	86.9	71.4	201.9
	Cst Pln (o)	154.6	172.4	665.0	149.3	728.9	1168.3
	Pied Low	102.6	270.6	450.8	215.4	96.9	110.2
	Pied Up	630.2	51.3	322.8	37.2	92.5	97.9
	Val Ridge (k)	345.7	651.5	410.8	349.8	612.3	436.9
	Val Ridge	141.4	343.8	104.4	67.2	124.1	144.9
Median	App Plat (g)	-140.0	-2444.0	-167.1	-162.3	-191.2	-182.9
	Blue Ridge	-259.4	-1173.8	-541.1	-337.2	-131.1	-1240.2
	Cst Pln (i)	-1.3	-17.4	0.0	-17.4	-2.6	-14.8
	Cst Pln (o)	-0.9	0.2	-50.5	0.2	-1.9	-858.8
	Pied Low	-0.6	-64.5	-4.8	-42.0	-1.7	-1.4
	Pied Up	-30.0	-5.6	0.0	-5.2	-2.6	-5.8
	Val Ridge (k)	28.2	64.1	25.3	11.7	42.0	-60.4
	Val Ridge	-85.4	-176.3	73.1	-9.0	-79.3	-104.5
Mean	App Plat (g)	-213.4	-2296.4	-726.6	-208.3	-315.1	-291.5
	Blue Ridge	-439.8	-1003.9	-858.7	903.3	-317.5	-967.3
	Cst Pln (i)	-36.7	0.6	-86.8	-49.4	3.6	-48.1
	Cst Pln (o)	12.6	40.3	-262.5	17.2	-190.4	-869.5
	Pied Low	-3.1	-111.5	-212.7	-86.4	-14.1	-3.7
	Pied Up	-213.6	-18.2	-110.1	-13.9	-3.7	-22.1
	Val Ridge (k)	175.8	-23.5	-5.9	172.1	12.1	-2.2
	Val Ridge	-107.4	-270.9	47.4	-36.1	-86.2	-109.6
SD	App Plat (g)	172.3	1374.7	1368.3	167.4	431.7	471.9
	Blue Ridge	612.0	1037.8	1226.9	5924.7	458.1	670.7
	Cst Pln (i)	59.5	238.8	136.1	72.8	72.7	199.9
	Cst Pln (o)	160.9	175.1	638.2	154.9	734.9	815.0
	Pied Low	105.7	254.1	409.7	203.4	98.8	113.5
	Pied Up	600.5	48.6	307.3	35.0	93.6	96.6
	Val Ridge (k)	311.0	680.0	429.0	318.2	639.4	456.3
	Val Ridge	96.5	222.0	97.6	59.5	93.6	99.4
Freq Omit	App Plat (g)	0.64	0.93	0.79	0.71	0.86	0.79
	Blue Ridge	0.80	0.80	0.80	0.67	0.87	0.53
	Cst Pln (i)	0.19	0.11	0.26	0.19	0.07	0.04
	Cst Pln (o)	0.17	0.08	0.42	0.08	0.92	0.33
	Pied Low	0.12	0.47	0.47	0.35	0.18	0.12
	Pied Up	0.20	0.08	0.18	0.03	0.13	0.08
	Val Ridge (k)	0.00	0.33	0.25	0.00	0.42	0.25
	Val Ridge	0.36	0.73	0.09	0.18	0.55	0.45
Freq Commit	App Plat (g)	0.00	0.00	0.00	0.00	0.07	0.00
	Blue Ridge	0.13	0.13	0.20	0.13	0.00	0.00
	Cst Pln (i)	0.00	0.04	0.00	0.00	0.04	0.07
	Cst Pln (o)	0.08	0.17	0.08	0.08	0.08	0.08
	Pied Low	0.12	0.12	0.06	0.06	0.18	0.12
	Pied Up	0.00	0.00	0.00	0.00	0.08	0.10
	Val Ridge (k)	0.33	0.42	0.25	0.33	0.42	0.42
	Val Ridge	0.00	0.00	0.36	0.00	0.00	0.00

*Curvature, openness, and GeoChan skeltons reduced using flow accumulationmap and size threshol; GeoVal map reduced with a valley extent and size threshold.

B2: Channel head detection statistics by land use

Appendix B2. Comparison of distances (in meters) between 148 observed channel head locations and 6 detection skeletons* from 14 sites in three land use contexts across the Chesapeake Bay Basin. Omissions and commissions refer to map under and over-estmates, respectively.

Statistic	Land Use	Curvature	NegOpen	PosOpen	CmbOpen	GeoChan	GeoVal
RMSE	Agriculture	621.7	91.4	1240.2	58.5	443.2	455.2
	Forest	463.2	1311.3	541.8	257.4	244.1	313.6
	Urban	89.6	198.1	143.1	144.6	97.0	100.8
Median	Agriculture	-30.0	-6.8	-26.6	-12.1	7.5	-39.3
	Forest	-41.5	-94.1	-57.3	-35.1	-34.6	-69.2
	Urban	-17.5	-9.6	0.0	-8.6	-2.4	-1.4
Mean	Agriculture	-278.8	-30.0	-527.1	-27.3	-81.3	-140.3
	Forest	-126.4	-622.8	-209.9	-67.6	-68.4	-109.6
	Urban	-28.6	2.1	-56.5	-45.9	6.2	7.3
SD	Agriculture	574.0	89.2	1159.4	53.4	450.0	447.2
	Forest	449.3	1163.4	503.6	250.4	236.3	296.2
	Urban	86.0	200.6	133.2	138.8	98.0	101.8
Freq Omit	Agriculture	0.25	0.13	0.38	0.06	0.19	0.06
	Forest	0.32	0.50	0.42	0.31	0.42	0.35
	Urban	0.20	0.15	0.22	0.20	0.10	0.07
Freq Commit	Agriculture	0.00	0.00	0.00	0.00	0.06	0.19
	Forest	0.06	0.08	0.08	0.06	0.10	0.08
	Urban	0.05	0.07	0.02	0.02	0.15	0.12

*Curvature, openness, and GeoChan skeltons reduced using flow accumulationmap and size threshol; GeoVal map reduced with a valley extent and size threshold.

B3: Channel head detection statistics by site

Appendix B3. Comparison of distances (in meters) between 148 observed channel head locations and 6 detection skeletons* from 14 sites across the Chesapeake Bay Basin. Omissions and commissions refer to map under and over-estmates, respectively.

Statistic	Site Name	Curvature	NegOpen	PosOpen	CmbOpen	GeoChan	GeoVal
RMSE	Blackbird	154.6	172.4	665.0	149.3	728.9	1168.3
	Catoctin	736.9	1418.8	1463.7	5794.7	544.7	1164.3
	Cornell	108.4	1335.1	1854.1	139.7	720.8	740.1
	Fair Hill	30.7	38.4	37.8	17.0	38.5	41.8
	Gettysburg	1242.4	73.0	1005.1	109.9	158.9	165.8
	Green Ridge	141.4	343.8	104.4	67.2	124.1	144.9
	Gunpowder	978.2	79.5	41.6	16.7	79.9	79.4
	Hammond	345.2	3310.9	1178.1	326.8	294.8	315.9
	Herbert Run	94.7	17.3	79.4	8.8	103.6	112.9
	Ltl Difficult Run	107.9	111.7	102.5	256.0	94.1	114.7
	Odenton	66.7	312.8	205.0	95.1	92.0	73.6
	Patuxent	71.8	34.9	67.6	75.4	29.9	291.5
	Ravensburg	345.7	651.5	410.8	349.8	612.3	436.9
	Sopers Branch	92.2	429.7	746.0	106.7	101.8	101.4
Median	Blackbird	-0.9	0.2	-50.5	0.2	-1.9	-858.8
	Catoctin	-259.4	-1173.8	-541.1	-337.2	-131.1	-1240.2
	Cornell	-100.3	-1321.9	-145.2	-138.8	-143.5	-142.8
	Fair Hill	-23.4	-4.0	2.8	-6.0	1.9	-33.6
	Gettysburg	-978.4	-28.9	-781.3	-30.4	129.3	-47.1
	Green Ridge	-85.4	-176.3	73.1	-9.0	-79.3	-104.5
	Gunpowder	-13.2	-1.8	-0.5	-1.8	-8.2	-7.7
	Hammond	-357.9	-3508.4	-310.6	-270.5	-264.3	-264.3
	Herbert Run	-35.5	-6.6	1.4	-4.9	-2.9	-1.4
	Ltl Difficult Run	1.0	-1.8	2.0	-8.7	-0.6	0.1
	Odenton	-14.7	-17.4	-26.9	-17.4	-5.0	-5.0
	Patuxent	-0.5	-18.7	0.0	-18.7	-0.7	-25.3
	Ravensburg	28.2	64.1	25.3	11.7	42.0	-60.4
	Sopers Branch	-38.5	-177.6	-573.1	-67.3	-51.5	-51.5
Mean	Blackbird	12.6	40.3	-262.5	17.2	-190.4	-869.5
	Catoctin	-439.8	-1003.9	-858.7	903.3	-317.5	-967.3
	Cornell	-93.5	-1232.9	-849.5	-130.4	-394.2	-410.6
	Fair Hill	-19.0	0.1	-11.7	-8.3	-9.3	-16.6
	Gettysburg	-1060.3	-42.8	-942.9	-72.1	135.2	-69.3
	Green Ridge	-107.4	-270.9	47.4	-36.1	-86.2	-109.6
	Gunpowder	-319.2	-38.5	-5.1	-8.7	-42.1	-41.8
	Hammond	-303.4	-3093.9	-634.5	-266.7	-255.8	-202.2
	Herbert Run	-60.2	-11.6	-30.0	-5.9	-10.9	-0.4
	Ltl Difficult Run	26.1	-4.1	4.3	-88.2	15.9	31.7
	Odenton	-37.1	20.4	-127.6	-54.9	16.1	-2.7
	Patuxent	-36.2	-24.2	-35.9	-42.6	-12.0	-104.7
	Ravensburg	175.8	-23.5	-5.9	172.1	12.1	-2.2
	Sopers Branch	-56.6	-308.5	-610.3	-83.0	-69.0	-68.5

Appendix B3 (continued). Comparison of distances (in meters) between 148 observed channel head locations and 6 detection skeletons* from 14 sites across the Chesapeake Bay Basin. Omissions and commissions refer to map under and over-estmates, respectively. (continued)

Statistic	Site Name	Curvature	NegOpen	PosOpen	CmbOpen	GeoChan	GeoVal
Freq Omit	Blackbird	0.17	0.08	0.42	0.08	0.92	0.33
	Catoctin	0.80	0.80	0.80	0.67	0.87	0.53
	Cornell	0.50	1.00	0.67	0.67	0.83	0.67
	Fair Hill	0.00	0.00	0.09	0.00	0.00	0.00
	Gettysburg	1.00	0.25	1.00	0.25	0.50	0.00
	Green Ridge	0.36	0.73	0.09	0.18	0.55	0.45
	Gunpowder	0.10	0.20	0.10	0.00	0.20	0.20
	Hammond	0.75	0.88	0.88	0.75	0.88	0.88
	Herbert Run	0.20	0.00	0.07	0.00	0.07	0.07
	Ltl Difficult Ru	0.09	0.27	0.18	0.36	0.18	0.09
	Odenton	0.27	0.20	0.40	0.27	0.07	0.07
	Patuxent	0.08	0.00	0.08	0.08	0.08	0.00
	Ravensburg	0.00	0.33	0.25	0.00	0.42	0.25
	Sopers Branch	0.17	0.83	1.00	0.33	0.17	0.17
Freq Commit	Blackbird	0.08	0.17	0.08	0.08	0.08	0.08
	Catoctin	0.13	0.13	0.20	0.13	0.00	0.00
	Cornell	0.00	0.00	0.00	0.00	0.00	0.00
	Fair Hill	0.00	0.00	0.00	0.00	0.00	0.00
	Gettysburg	0.00	0.00	0.00	0.00	0.25	0.75
	Green Ridge	0.00	0.00	0.36	0.00	0.00	0.00
	Gunpowder	0.00	0.00	0.00	0.00	0.00	0.00
	Hammond	0.00	0.00	0.00	0.00	0.13	0.00
	Herbert Run	0.00	0.00	0.00	0.00	0.13	0.07
	Ltl Difficult Ru	0.18	0.18	0.09	0.09	0.27	0.18
	Odenton	0.00	0.07	0.00	0.00	0.07	0.13
	Patuxent	0.00	0.00	0.00	0.00	0.00	0.00
	Ravensburg	0.33	0.42	0.25	0.33	0.42	0.42
	Sopers Branch	0.00	0.00	0.00	0.00	0.00	0.00

*Curvature, openness, and GeoChan skeltons reduced using flow accumulationmap and size threshol; GeoVal map reduced with a valley extent and size threshold.

B4: Channel head detection graphical summary by site

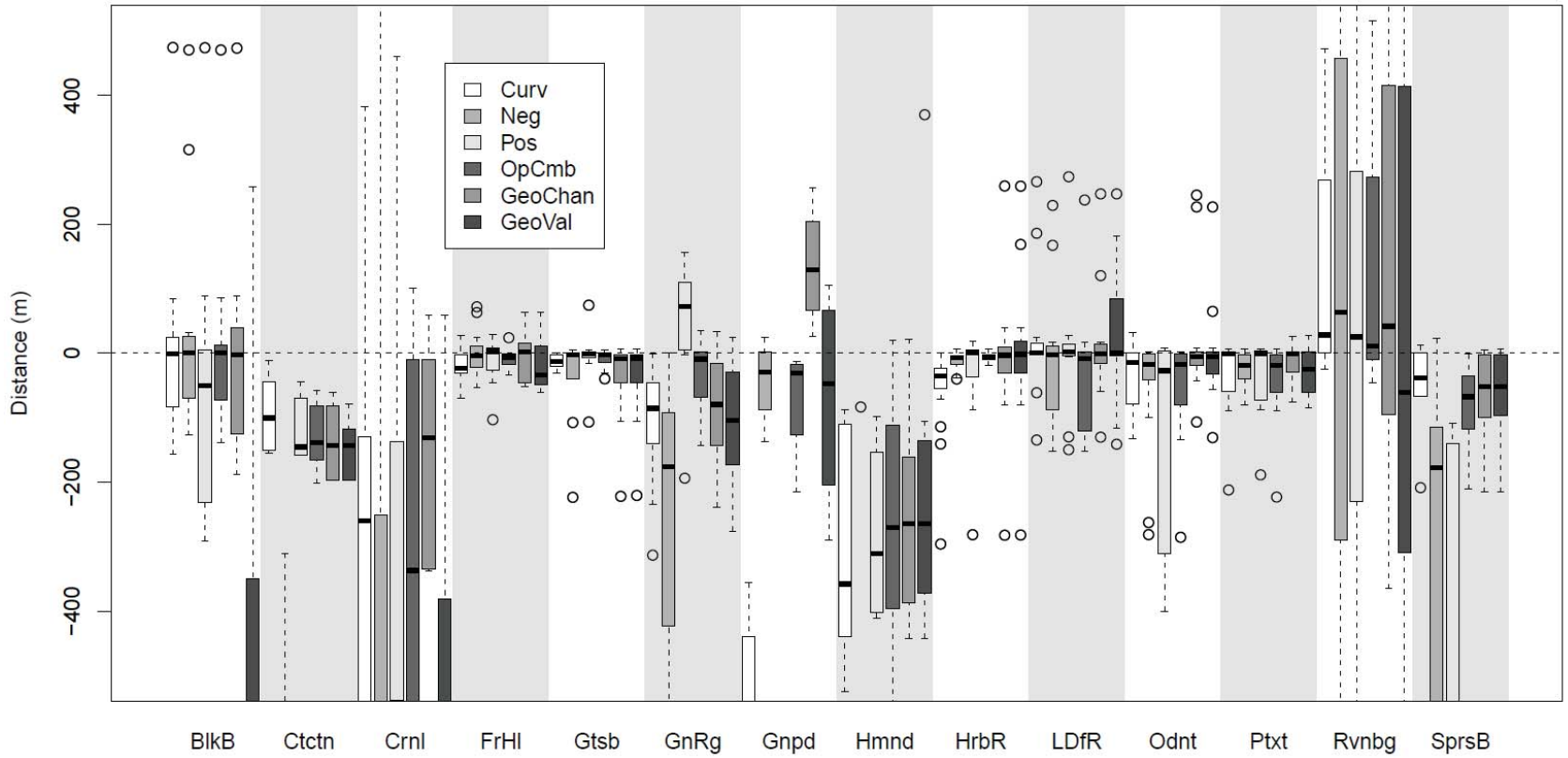

Appendix C

C1: Percentage of landscape pixels removed by geomorphic and cartographic elimination